Probing topological states through the exact non-Markovian decoherence dynamics of a spin coupled to a spin bath in the real-time domain

Chuan-Zhe Yao and Wei-Min Zhang*

Department of Physics and Center for Quantum Information Science, National Cheng Kung University, Tainan 70101, Taiwan

(Received 14 April 2020; revised 14 June 2020; accepted 2 July 2020; published 20 July 2020)

In this paper, we explore the decoherence dynamics of a probing spin coupled to a spin bath, where the spin bath is given by a controllable 1D transverse-field Ising chain. The 1D transverse-field Ising chain with free-end boundary condition is equivalent to a modified Kitaev model with nonlocal Majorana bound states in its topological phase. We find that the non-Markovian decoherence dynamics of the probing spin can manifest the topological structure of the spin chain. By controlling the external magnetic field on the Ising chain, we find a close relationship between the topological phase transition and the non-Markovian dynamics in the real-time domain. We also investigate the corresponding quantum entanglement dynamics in this topological system.

DOI: 10.1103/PhysRevB.102.035133

I. INTRODUCTION

In condensed matter physics, the transverse-field Ising model (equivalently the Heisenberg-Ising chain) not only allows identification of quantum phase transitions [1,2] but also has been experimentally realized through the $CoNb_2O_6$ compound [3], trapped ions [4–7], Mott insulator [8], and Rydberg atom [9] etc., and therefore it has been widely investigated. On the other hand, recent experiments with polar molecules and ion chains provide a new direction for the dynamics of many-body systems in the real-time domain. In particular, the transverse-field Ising model has been revisited in the investigation of nonequilibrium physics, such as dynamical quantum phase transition, through the time evolution of observables in the transverse-field Ising chain under dynamical quench [10–13], the Loschmidt echo of a probing spin homogeneously coupled to a transverse-field Ising chain [14–16], and the decoherence dynamics of a transverse-field Ising chain coupled to a thermal bath [17,18]. However, most of these investigations are mainly considered for Markov processes, while the dynamics of many open systems are often non-Markovian dominated. In this paper, we shall investigate the real-time non-Markovian dynamics for a transverse-field Ising model in different quantum phases with different initial states, through its coupling to a probing spin.

As it is well known, by Jordan-Wigner transformation, the transverse-field Ising model can be mapped onto the Kitaev chain model [19–22]. In the fermionic representation, the well-known quantum phase transition of the model can be understood as a transition from the weak-pairing BCS regime to the strong-pairing Bose-Einstein condensate regime [23,24]. The phase diagram can be classified according to the topological order [23–26]. Moreover, the Kitaev model possesses Majorana zero modes (Majorana bound states) nonlocally separated at the two ends of the open chain in the topologically nontrivial phase. The dynamical behavior of quantum phase transition in the model must relate topologically to the nonlocal property of the Majorana zero modes. However, the previous studies mainly consider the transverse-field Ising model with periodic boundary condition where the Majorana zero modes cannot be manifested. Meanwhile, even though the solution of the transverse-field Ising model with free-end boundary condition is exactly solvable, its eigenenergies and eigenfunctions are determined by a transcendental equation which has not been analytically solved so far [1,2,18].

In this paper, we will modify the transverse-field Ising model such that the local magnetic field does not apply to the last spin of the Ising chain. We find that such a modified model can be solved analytically with the free-end boundary condition for the eigenenergies and eigenfunctions. Moreover, we derive the exact master equation of a probing spin coupled to the transverse-field Ising model [27–35]. Through the investigation of non-Markovian dynamics of the probing spin coupled to this modified transverse-filed Ising chain, one can probe experimentally, for example with Ramsey interferometry, how the nontrivial topological properties of the transverse-filed Ising model can be manifested in the real-time domain. A great number of papers have been devoted to the study entanglement close to topological phase transition, and there have been indications that entanglement is enhanced near the quantum critical point [36–39]. We also numerically explore the non-Markovian dynamics of the entanglement entropy which shows a diagnostic tool for the study of topological phase transitions.

The rest of the paper is organized as follows. In Sec. II, we introduce our modified transverse-field Ising model and study its topological characterization. In Sec. III, we derive the exact master equation of a probing spin coupled to the modified transverse-field Ising model by using the path integral approach in the coherent state representation [27]. In Sec. IV, we analyze in detail the non-Markovian decoherence dynamics of the probing spin coupled to the modified transverse-field

*wzhang@mail.ncku.edu.tw

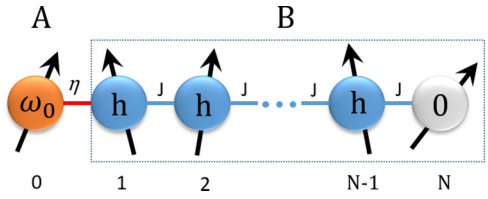

FIG. 1. A schematic diagram of the probing spin coupled to the modified transverse-field Ising chain with setting the parameters of the coupling constant and the external magnetic field as in Eq. (1).

Ising model by investigating two-time spin-spin correlation functions in different phases of the spin chain, different spin-spin chain coupling, different spin-flip energy, and different initial states. The effects of topologically nonlocal property on the non-Markovian dynamics are also clarified under different conditions. In Sec. V, we solve the dynamics of the entanglement entropy through the exact master equation in Sec. III. We also find the close relationships between the dynamical entanglement entropy and the topological phase transition in the real-time domain. The relation between the entanglement entropy and the two-time spin-spin correlation obtained in Sec. IV is also presented. Finally, a conclusion is given in Sec. VI. The detailed derivations of the formulas are presented in the appendices.

II. THE MODIFIED TRANSVERSE-FIELD ISING MODEL AND ITS TOPOLOGICAL STRUCTURE

To probe topological structure and dynamical phase transition through non-Markovian decoherence dynamics and entanglement entropy in the real-time domain, we couple a probing spin to a modified 1D transverse-field Ising chain as shown in Fig. 1. The Hamiltonian of the system is

$$\begin{aligned} H &= H_A + H_I + H_B \\ &= -\omega_0\sigma_0^z - \eta\sigma_0^x\sigma_1^x - \sum_{j=1}^{N-1} J_j\sigma_j^x\sigma_{j+1}^x - \sum_{j=1}^{N} h_j\sigma_j^z, \end{aligned} \tag{1}$$

where the first term is the Hamiltonian of the probing spin σ_0, and the second term is the coupling between the probing spin σ_0 and the first spin σ_1 in the modified transverse-field Ising chain. The last two terms are the Hamiltonian of the modified 1D transverse-field Ising model, which is an N-site spin chain with the nearest coupling J_j and the local external magnetic field h_j with $\sigma_j^{x,y,z}$ being the Pauli matrices. Different from the previous works on the conventional transverse-field Ising chain with a period boundary condition, here we set the transverse-field Ising chain to have a free-end boundary condition so that its topological features can be presented on the edge. However, as shown as early by Lieb *et al.* [1] and later by Pfeuty [2], although the transverse-field Ising model with free ends is exactly solvable, its eigenenergies and eigenfunctions are determined by a transcendental equation which cannot be solved analytically. Hence, we modify the model by setting $h_N = 0$, namely, the local magnetic fields do not apply to the spin σ_N at last site. This modification makes the free-boundary transverse-field Ising chain analytically solvable, and meantime the topological structure of the system can still be maintained as we will show later. The spin-flip energy ω_0 of the probing spin σ_0 and the coupling energy η between σ_0 and σ_1 are controllable. For simplicity, we also set $J_i = J$, $h_i = h$ $(i = 1, \ldots, N-1)$.

By applying the Jordan-Wigner transformation

$$\sigma_j^+ = \left(\sigma_j^x + i\sigma_j^y\right)/2 = c_j^\dagger \prod_{m<j} e^{-i\pi c_m^\dagger c_m} \tag{2a}$$

$$\sigma_j^- = \left(\sigma_j^x - i\sigma_j^y\right)/2 = c_j \prod_{m<j} e^{i\pi c_m^\dagger c_m} \tag{2b}$$

$$\sigma_j^z = 2c_j^\dagger c_j - 1, \tag{2c}$$

the total system can be transformed into a fermionic system:

$$\begin{aligned} H = &-\omega_0(2a^\dagger a - 1) - \eta(a^\dagger - a)(c_1^\dagger + c_1) \\ &- \sum_{j=1}^{N-1}(Jc_j^\dagger c_{j+1}^\dagger + Jc_j^\dagger c_{j+1} + hc_j^\dagger c_j + \text{H.c.}). \end{aligned} \tag{3}$$

Here we have ignored a constant term in the above Hamiltonian. As it is shown, after the Jordan-Wigner transformation, the transverse-field Ising chain is reduced to the Kitaev chain with the same hopping and pairing strengths [1,2,19,24], except that the onsite chemical potential of the last site, $j = N$, vanishes as an effect of the modification of the model, see Eq. (3). We take further a Bogoliubov transformation to the spin chain

$$b_k = \sum_{i=1}^{N}(u_{ki}c_i + v_{ki}c_i^\dagger) \tag{4a}$$

$$b_k^\dagger = \sum_{i=1}^{N}(v_{ki}^* c_i + u_{ki}^* c_i^\dagger), \tag{4b}$$

such that H_B is diagonalized,

$$H_B = \sum_k \epsilon_k(b_k^\dagger b_k - b_k b_k^\dagger), \tag{5}$$

where b_k and $b_k^\dagger$ are creation and annihilation operators of Bogoliubov quasiparticles (bogoliubons) with the spectrum

$$\epsilon_k = \begin{cases} J\sqrt{1+\lambda^2-2\lambda\cos\frac{k\pi}{N}}, & k = 1, 2, \ldots, N-1 \\ 0, & k = k_0 \end{cases}, \tag{6}$$

where $\lambda = h/J$, and the zero energy mode k_0 is determined by $1 + \lambda^2 - 2\lambda\cos\frac{k_0\pi}{N} = 0$. The corresponding wave functions for the nonzero energy bogoliubons can be analytically solved

$$u_{kj} = \mathcal{N}_k\left\{\frac{-J}{\epsilon_k}\sin\left[\frac{(j-1)k\pi}{N}\right] + \left(1 - \frac{J\lambda}{\epsilon_k}\right)\sin\frac{jk\pi}{N}\right\}, \tag{7a}$$

$$v_{kj} = \mathcal{N}_k\left\{\frac{-J}{\epsilon_k}\sin\left[\frac{(j-1)k\pi}{N}\right] - \left(1 + \frac{J\lambda}{\epsilon_k}\right)\sin\frac{jk\pi}{N}\right\}, \tag{7b}$$

and that of the zero-energy bogoliubon is

$$u_{k_0 j} = \begin{cases} \mathcal{N}_{k_0}(-\lambda)^{j-1} & j < N \\ \mathcal{N}_{k_0}(-\lambda)^{N-1} + 1/2 & j = N \end{cases} \tag{8a}$$

$$v_{k_0 j} = \begin{cases} \mathcal{N}_{k_0}(-\lambda)^{j-1} & j < N \\ \mathcal{N}_{k_0}(-\lambda)^{N-1} - 1/2 & j = N \end{cases}, \tag{8b}$$

where $\mathcal{N}_k, \mathcal{N}_{k_0}$ are the normalization constants which are given by

$$\mathcal{N}_k = \left\{ N\left[1 + 2\frac{J^2}{\epsilon_k^2}\left(1 + \cos\frac{k\pi}{N}\right)\right]\right\}^{-1/2} \tag{9a}$$

$$\mathcal{N}_{k_0} = \frac{1}{2}\left(\frac{1-\lambda^{2N}}{1-\lambda^2}\right)^{-1/2}. \tag{9b}$$

The detailed derivation is given in Appendix A. Thus, the Hamiltonian of Eq. (1) can be expressed as

$$H = -\omega_0(2a^\dagger a - 1) - \sum_k V_k(a^\dagger - a)(b_k^\dagger + b_k) + \sum_k \epsilon_k(2b_k^\dagger b_k - 1), \tag{10}$$

with

$$V_k = \begin{cases} \frac{-2\eta\lambda\sin\frac{k\pi}{N}}{\sqrt{N(1+\lambda^2-2\lambda\cos\frac{k\pi}{N})}}, & k = 1, 2, \ldots, N-1 \\ \sqrt{2}\eta\left(\sum_{j=0}^{N-1}\lambda^{2j}\right)^{-1/2}, & k = k_0 \end{cases}. \tag{11}$$

The above analytical solution, Eqs. (6)–(8), is in fact a consequence of the modification with $h_N = 0$. In the case of $h_N = h$, no such analytical solution has been found in the literature (see Appendix A). Meanwhile, the modified transverse-field Ising chain has some different characters from the Kitaev chain. The difference is manifested first in the spectra of the model with and without setting $h_N = 0$, as shown in Figs. 2(a) and 2(b), respectively. The resulting excited state spectra are similar for the two cases, but their ground state behavior is very different. The modified model always has zero-energy states, independent of the value of λ, while the zero-energy states only exist in the region of $\lambda < 1$ for large N in the ordinary transverse-field Ising chain (or the equivalent Kitaev chain).

Secondly and more importantly, the wave-function distribution of the ground states in the two cases are significantly different, except for $\lambda = 0$ (no transverse field), as shown in Figs. 2(c$_1$)-(c$_2$) and 2(d$_1$)-(d$_2$). Note that the zero-energy bogoliubon state ($\epsilon_k = 0$) is twofold degenerate, with the particle number $b_0^\dagger b_0 = 0$ and 1, respectively. These two states can be described by the left and right Majorana operators $\gamma_L = -i(b_0 - b_0^\dagger)$, $\gamma_R = b_0 + b_0^\dagger$ [19]. Figure 2(c$_1$)–(c$_2$) demonstrates the nonlocal separation of the two Majorana zero modes in the topologically nontrivial phase ($\lambda < 1$), distributed asymmetrically in the two sides of the spin chain. In particular, if $\lambda = 0$, these two Majorana zero modes locate perfectly at the end of the two sides of the spin chain, just the same as that in the Kitaev model [19]. As λ gets increased, only the left Majorana zero mode wave function spreads into other sites, while the right Majorana zero mode remains unchanged due to the setting $h_N = 0$, as shown in Fig. 2(c$_1$)-(c$_2$). At the critical point $\lambda_c = 1$, the left Majorana zero mode wave function is uniformly distributed over all sites of the chain but the right Majorana zero mode still remains unchanged. However, for the Kitaev chain, the wave function of the left and right Majorana zero modes are symmetrically distributed over the chain for $\lambda < 1$, see Fig. 2(d$_1$)-(d$_2$). By comparing Fig. 2(c$_1$)-(c$_2$) with Fig. 2(d$_1$)-(d$_2$), we find that the wave-function distribution of the left Majorana zero mode is the same for $\lambda < 1$ in both cases, but the wave-function distribution of the right Majorana zero mode is very different. When $\lambda > 1$, for the modified transverse-field Ising chain, the wave function of the left Majorana zero mode distributes more on the right-hand side (r.h.s.) than the left-hand side (l.h.s.). With continuously increasing λ, the left Majorana zero mode γ_L eventually condenses with the right Majorana zero mode γ_R to the last site N so that the Majorana zero modes still exist but no longer have the topologically nonlocal property. This solution ($\lambda > 1$) of the modified Ising chain is very different from the Kitaev model in which there exists no longer a zero-energy state for $\lambda > 1$, as shown in Fig. 2.

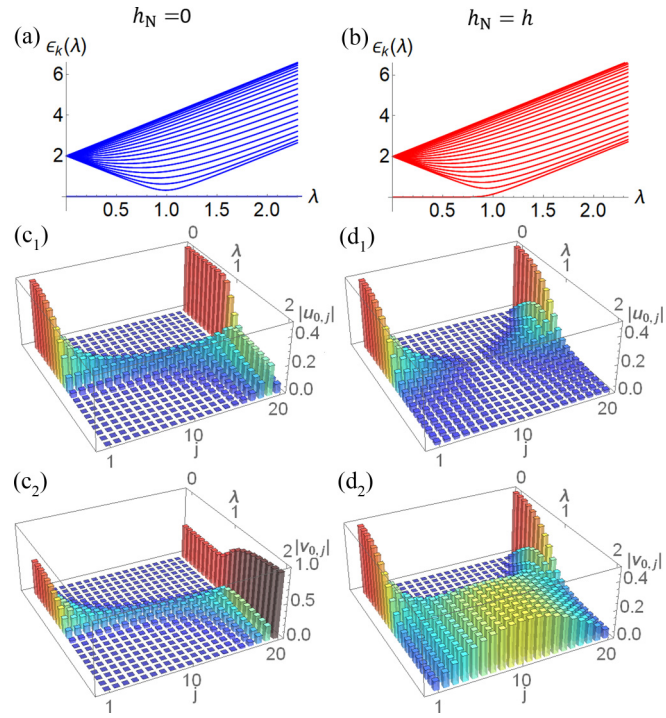

FIG. 2. The spectrum for (a) the modified transverse-field Ising chain ($h_N = 0$) and (b) the ordinary transverse-field Ising chain ($h_N = h$) with $N = 20$. The wave-function distribution of the ground state, $|u_{0,j}|$ (top) and $|v_{0,j}|$ (bottom) for (c) $h_N = 0$ and (d) $h_N = h$ with varying from the topologically nontrivial phase $\lambda = 0$ to the topologically trivial phase $\lambda = 2$.

We summarize the above topological properties of the modified transverse-field Ising chain as follows: The condition $h_N = 0$ makes the right Majorana zero mode always localize at the end of the r.h.s. of spin chain, independent of the value of λ. Meanwhile, the wave-function distribution of the left Majorana zero mode changes and moves from the l.h.s. to the r.h.s. of the spin chain when the parameter λ changes from $\lambda < 1$ to $\lambda > 1$, which results in a topological phase transition at the critical point $\lambda_c = 1$. This topological

phase transition remains unchanged even in the limit $N \to \infty$, because it is the local and nonlocal topological properties of the Majorana zero mode wave functions associated with the ends of the spin chain rather than its length. In fact, this topological feature becomes more significant for the larger N, where the nonlocality of Majorana zero modes is manifested clearer [19]. On the other hand, practically h_N may not be ideally zero, i.e., it may have some small but nonzero local transverse field h_N in experiments. However, a very small h_N only causes a very small tail to the wave-function distribution of the right Majorana zero mode over a couple of sites from the right end of the spin chain. This small wave-function tail does not change the above topological feature, as an evidence of topological protection from local perturbation [19].

The above topological properties of the zero-energy states can be understood more comprehensively through calculating the winding number, which is used to identify topological phases of matter [24,26,40,41]. To this end, we rewrite the Hamiltonian of the spin chain in Eq. (10) in the pseudo spin representation:

$$H_B = \sum_k (c_k^\dagger \quad c_k) P^{-1} \begin{pmatrix} z(k) & x(k) \\ x(k) & -z(k) \end{pmatrix} P \begin{pmatrix} c_k \\ c_k^\dagger \end{pmatrix}, \tag{12}$$

where

$$P = \begin{pmatrix} z(k) - \sqrt{z^2(k)+x^2(k)} & x(k) \\ z(k) + \sqrt{z^2(k)+x^2(k)} & x(k) \end{pmatrix} \tag{13}$$

and

$$x(k) = J \sin(k\pi/N) \tag{14a}$$

$$z(k) = J\cos(k\pi/N) - h + (h-j)\delta_{k,k_0}. \tag{14b}$$

The winding number is defined as the line integral along a close curve on the z-x plane

$$W = \frac{1}{2\pi} \int_c \frac{1}{x^2+z^2}(z dx - x dz), \tag{15}$$

as the total number of times that the curve travels counterclockwise around the origin. Explicit calculation shows that the winding number $W = 1$ for $\lambda < 1$, which means that the spin chain is in the topologically nontrivial phase, while it is in the topologically trivial phase with $W = 0$ for $\lambda > 1$, although there is still zero-energy ground state. This demonstrates a topological phase transition in the modified transverse-field Ising chain associated with the topological nonlocal feature, namely, a transition from the topologically nontrivial phase to the topologically trivial phase occurs when λ passes through $\lambda_c = 1$.

In conclusion, the modified transverse-field Ising chain exhibits a similar topological phase transition as the ordinary transverse-field Ising chain, but the ground state energy and its wave functions behave so differently in the two models. It also demonstrates explicitly that the topology of the system is determined by the detailed nonlocal properties of the zero-mode wave functions, rather than the system spectra. Because the modified transverse-field Ising model can be analytically solved explicitly for both the eigenenergies and eigenfunctions, we can also use it to study the exact decoherence dynamics of the system through its coupling to a probing spin, which is fully encapsulated in the spectral density $J(\omega) \equiv 2\pi \sum_k |V_k|^2 \delta(\omega_k - \omega) = 2\pi\rho(\omega)|V(\omega)|^2$. Here $\rho(\omega)$ is the density of states of the spin chain that can be determined from Eq. (6), and $V(\omega)$ is the coupling amplitude of the probing spin coupled to the spin chain that involves explicitly all the eigenfunction distributions of the spin chain as given by Eq. (11). This indicates that the topological properties of the spin chain can be experimentally observed from the decoherence dynamics of the probing spin, as we shall show in the next sections.

III. THE EXACT MASTER EQUATION

The topological properties and topological phase transition of the modified Ising chain can be explored through the non-Markovian decoherence dynamics of the probing spin, which is described by the time evolution of the reduced density matrix of the probing spin. The reduced density matrix is obtained from the total density matrix of the probing spin and the spin chain by tracing out all possible states of the spin chain

$$\rho_A(t) = \mathrm{Tr}_B[U(t,t_0)\rho_{\mathrm{tot}}(t_0)U^\dagger(t,t_0)], \tag{16}$$

where $U(t,t_0) = \exp[-iH(t-t_0)]$ is the time evolution operator of the total system. Initially we assume that the two subsystem (spin σ_0 and the spin chain) are decoupled [42,43], that is, $\rho_{\mathrm{tot}}(t_0) = \rho_A(t_0) \otimes \rho_B(t_0)$. Then in the fermionic coherent state representation

$$\langle \xi_f | \rho_A(t) | \xi_f' \rangle = \int d\mu(\xi_0) d\mu(\xi_0') \langle \xi_0 | \rho_A(t_0) | \xi_0' \rangle \mathcal{K}(\xi_f^*, \xi_f', t | \xi_0, \xi_0'^*, t_0), \tag{17}$$

where ξ_0, $\xi_0'^*$, ξ_f', ξ_f^* are the eigenvalues of the fermionic coherent states and are Grassmann numbers. The propagator $\mathcal{K}(\xi_f^*, \xi_f', t|\xi_0, \xi_0'^*, t_0)$ is determined by the action of the probing spin σ_0 and the influence functional arose from the spin chain [42]; the latter is obtained by integrating out all the degree of freedom of the spin chain [27–35]. With a tedious derivation (see Appendix B), the exact master equation for the probing spin coupling to the transverse-field Ising chain is obtained

$$\begin{aligned} \dot\rho_A(t) = &-i[\epsilon(t,t_0)a^\dagger a, \rho_A(t)] \\ &+ \gamma(t,t_0)[2a\rho_A(t)a^\dagger - a^\dagger a\rho_A(t) - \rho_A(t)a^\dagger a] \\ &+ \tilde\gamma(t,t_0)[a^\dagger\rho_A(t)a - a\rho_A(t)a^\dagger + a^\dagger a\rho_A(t) \\ &- \rho_A(t)aa^\dagger] + \Lambda(t,t_0)a^\dagger\rho_A(t)a^\dagger \\ &+ \Lambda^*(t,t_0)a\rho_A(t)a, \end{aligned} \tag{18}$$

where all the time-dependent coefficients are determined by the generalized nonequilibrium Green functions incorporating the pairing dynamics as follows,

$$\epsilon(t,t_0) = \frac{i}{2}[\dot{\boldsymbol{U}}(t,t_0)\boldsymbol{U}^{-1}(t,t_0) - \mathrm{H.c.}]_{11}, \tag{19a}$$

$$\gamma(t,t_0) = -\frac{1}{2}[\dot{\boldsymbol{U}}(t,t_0)\boldsymbol{U}^{-1}(t,t_0) + \mathrm{H.c.}]_{11}, \tag{19b}$$

$$\tilde\gamma(t,t_0) = \dot{\boldsymbol{V}}_{11}(t,t) - [\dot{\boldsymbol{U}}(t,t_0)\boldsymbol{U}^{-1}(t,t_0)\boldsymbol{V}(t,t) + \mathrm{H.c.}]_{11}, \tag{19c}$$

$$\Lambda(t,t_0) = -[\dot{\boldsymbol{U}}(t,t_0)\boldsymbol{U}^{-1}(t,t_0)]_{12}. \tag{19d}$$

The Green functions $\boldsymbol{U}(t,t_0)$ and $\boldsymbol{V}(t,t)$ are 2×2 matrix and satisfy the integrodifferential equations [27–35]

$$\frac{d}{dt}\boldsymbol{U}(t,t_0)-2i\omega_0\begin{pmatrix}1&0\\0&-1\end{pmatrix}\boldsymbol{U}(t,t_0)+\int_{t_0}^{t}\boldsymbol{G}(t,\tau)\boldsymbol{U}(\tau,t_0)d\tau=0 \tag{20a}$$

$$\boldsymbol{V}(t,\tau)=\int_{t_0}^{\tau}d\tau_1\int_{t_0}^{t}d\tau_2\boldsymbol{U}(\tau,\tau_1)\tilde{\boldsymbol{G}}(\tau_1,\tau_2)\boldsymbol{U}^{\dagger}(t,\tau_2) \tag{20b}$$

with the initial condition $\boldsymbol{U}(t_0,t_0)=\boldsymbol{I}$. The integral memory kernels

$$\boldsymbol{G}(t,t_0)=2\,\mathrm{Re}[g(t,t_0)]\begin{pmatrix}1&-1\\-1&1\end{pmatrix} \tag{21a}$$

$$\tilde{\boldsymbol{G}}(t,t_0)=\{g(t,t_0)-2\,\mathrm{Im}[g_\beta(t,t_0)]\}\begin{pmatrix}1&-1\\-1&1\end{pmatrix}, \tag{21b}$$

where

$$g(t,t_0)=\int\frac{d\omega}{2\pi}J(\omega)e^{-i\omega(t-t_0)}, \tag{22a}$$

$$g_\beta(t,t_0)=\int\frac{d\omega}{2\pi}J(\omega)f(\omega)e^{-i\omega(t-t_0)}, \tag{22b}$$

and $f(\omega)=[e^{\beta(\epsilon_k-\mu)}+1]^{-1}$ is the Fermi-Dirac distribution of the spin chain at initial time t_0. The spectral density of the system,

$$J(\omega)\equiv2\pi\sum_k|V_k|^2\delta(\omega-\epsilon_k)=2\pi\rho(\omega)|V(\omega)|^2, \tag{23}$$

where V_k and ϵ_k are given by Eq. (11) and Eq. (6), respectively. The explicit form is given as follows,

$$J(\omega)=\frac{\eta^2}{\omega}\sqrt{-[\omega^2/4-J^2(1-\lambda)^2][\omega^2/4-J^2(1+\lambda)^2]}+\begin{cases}\pi\eta^2(1-\lambda^2)\delta_{\omega,0}&\lambda<1\\0&\lambda\geqslant1\end{cases}, \tag{24}$$

in which the last term is contributed from the nonlocal Majorana zero modes. Note that when $\lambda\geqslant1$, the zero modes have no contribution to the spectral density because the zero modes move to the right-hand side of the spin chain and therefore decouple from the probing spin. From Eqs. (20a) and (21a), it shows that the memory kernel is determined by the effective spectral density $\mathcal{J}(\lambda,\omega)=2\,\mathrm{Re}[J(\omega)]$ plotted in Fig. 3. Notice that except for the case of $\lambda=1$, there is a gap in the middle of the effective spectral density, which will induce localized bound states and prevent decoherence [31], as we will discuss in detail in the next section.

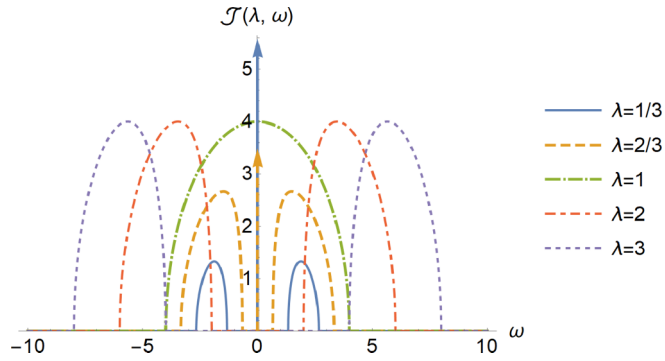

FIG. 3. The effective spectral density $\mathcal{J}(\lambda,\omega)$ from the topologically nontrivial phase ($\lambda<1$) to the topologically trivial phase ($\lambda>1$).

IV. THE EXACT NON-MARKOVIAN DYNAMICS

A. The analytical solution of the retarded and correlation Green functions

By coupling the probing spin σ_0 with the spin chain (see Fig. 1), we find that the dynamics of the probing spin manifest the topological properties of the spin chain. As one has seen, the renormalized Hamiltonian of the probing spin and the dissipation and fluctuation coefficients in its exact master equation Eq. (18) are all determined by the Green functions $\boldsymbol{U}(t,t_0)$ and $\boldsymbol{V}(t,t)$. The solutions of these two Green functions fully depend on the density of states of the spin chain as well as the coupling between the probing spin and the spin chain through the spectral density of Eq. (24). Their physical consequences can be seen more clearly in the Heisenberg picture. After the Jordan-Wigner transformation, the dynamics of the probing spin σ_0 is described by the corresponding fermion operators $a(t)$ and $a^\dagger(t)$. Their Heisenberg equations of motion, after eliminating the degrees of freedom of the spin chain, lead to

$$\frac{d}{dt}a(t)-2i\omega_0a(t)-2\int_{t_0}^{t}\mathrm{Re}[g(t,t_0)][a^\dagger(\tau)-a(\tau)]d\tau=\sum_k iV_k[e^{-2i\epsilon_kt}b_k(t_0)+e^{2i\epsilon_kt}b_k^\dagger(t_0)] \tag{25}$$

which is the generalized quantum Langevin equation [33], where the third term is a damping and the right-hand side of the equation is the noise force. Due to the linearity of Eq. (25), its general solution has the form as

$$\begin{pmatrix}a(t)\\a^\dagger(t)\end{pmatrix}=\boldsymbol{U}(t,t_0)\begin{pmatrix}a(t_0)\\a^\dagger(t_0)\end{pmatrix}+\sum_k\boldsymbol{F}_k(t,t_0)\begin{pmatrix}b_k(t_0)\\b_k^\dagger(t_0)\end{pmatrix}, \tag{26}$$

where $a(t_0)$, $a^\dagger(t_0)$, $b_k(t_0)$, and $b_k^\dagger(t_0)$ are related to the initial annihilation and creation operators of the probing spin σ_0 and the spin chain, respectively.

From Eq. (26), it can easily be shown that

$$\boldsymbol{U}(t,t_0)=\begin{pmatrix}\langle\{a(t),a^\dagger(t_0)\}\rangle&\langle\{a(t),a(t_0)\}\rangle\\\langle\{a^\dagger(t),a^\dagger(t_0)\}\rangle&\langle\{a^\dagger(t),a(t_0)\}\rangle\end{pmatrix} \tag{27}$$

which is indeed an extension of the usual retarded Green function incorporating with pairings. The equation of motion of $\boldsymbol{U}(t,t_0)$ is given by the integrodifferential Eq. (20a), which can also be easily justified by substituting Eq. (26) into the Heisenberg equation of motion (25). As shown in our previous work [31], the modified Laplace transform $\tilde{\boldsymbol{U}}(s)=\int_{t_0}^{\infty}\boldsymbol{U}(t,t_0)e^{is(t-t_0)}$ of Eq. (20a) is

$$\tilde{\boldsymbol{U}}(s)=i\begin{pmatrix}s+2\omega_0-\Sigma(s)&\Sigma(s)\\\Sigma(s)&s-2\omega_0-\Sigma(s)\end{pmatrix}^{-1}, \tag{28}$$

where the self-energy correction $\Sigma(s)$ is the Laplace transform of the integral kernel in Eq. (20a)

$$\Sigma(s)=\int\frac{d\omega}{2\pi}\frac{\mathcal{J}(\lambda,\omega)}{s-\omega}\xrightarrow{s=\omega\pm i0^+}\Delta(\lambda,\omega)\mp\frac{i}{2}\mathcal{J}(\lambda,\omega),\quad(29)$$

and $\Delta(\lambda,\omega)=\mathcal{P}\int\frac{d\omega}{2\pi}\frac{\mathcal{J}(\lambda,\omega)}{s-\omega}$ is the principal value of the integral. Applying the inverse transformation to Eq. (28), we can analytically solve $\boldsymbol{U}(t,t_0)$, which consists of a summation of dissipationless oscillations arose from localized modes (localized bound states) determined by the real part of the self-energy correction to the probing spin, plus nonexponential decays induced by the discontinuity of the imaginary part of the self-energy correction cross the real axes in the complex plane [31]

$$\begin{aligned}\boldsymbol{U}(t,t_0)=&\sum_{s_p}\begin{pmatrix}X(s_p)&Y(s_p)\\Y(s_p)&X(-s_p)\end{pmatrix}e^{-is_p(t-t_0)}\\&+\int_{-\infty}^{\infty}\frac{ds}{2\pi}\frac{\mathcal{J}(s)e^{-is(t-t_0)}}{\left[4\omega_0^2+(2\Delta(s)-s)s\right]^2+s^2(\mathcal{J}(s))^2}\\&\times\begin{pmatrix}(s-2\omega_0)^2&4\omega_0^2-s^2\\4\omega_0^2-s^2&(s+2\omega_0)^2\end{pmatrix},\end{aligned}\quad(30)$$

where $\{s_p\}$ is the set of the poles for the determinant of $\tilde{\boldsymbol{U}}(s)$ located at the real axis, i.e., $s-2\omega_0-\Delta(s_p)=0$, and

$$X(s)=\frac{[s-2\omega_0-\Delta(s)]^2}{[s-2\omega_0-\Delta(s)]^2+\Delta^2(s)-\Delta'(s)(s-2\omega_0)^2},\quad(31a)$$

$$Y(s)=\frac{\Delta^2(s)}{2\Delta(s)(\Delta(s)-s)+\Delta'(s)\left(s^2-4\omega_0^2\right)}.\quad(31b)$$

Both the dissipationless oscillations arose from the localized modes (localized bound states) and the nonexponential decays in Eq. (30) are fully determined by the spectral density.

On the other hand, $\{\boldsymbol{F}_k(t,t_0)\}$ in Eq. (26) is the noise source which characterizes the noise force, the right-hand side of Eq. (25) associated with the initial operators $\{b_k(t_0),b_k^\dagger(t_0)\}$ of the spin chain, and obeys the equation of the motion:

$$\begin{aligned}&\frac{d}{dt}\boldsymbol{F}_k(t,t_0)-2i\omega_0\begin{pmatrix}1&0\\0&-1\end{pmatrix}\boldsymbol{F}_k(t,t_0)\\&+\int_{t_0}^{t}\boldsymbol{G}(t,\tau)\boldsymbol{F}_k(\tau,t_0)d\tau=iV_k\begin{pmatrix}e^{-2i\epsilon_k\tau}&e^{2i\epsilon_k\tau}\\-e^{-2i\epsilon_k\tau}&-e^{2i\epsilon_k\tau}\end{pmatrix}.\end{aligned}\quad(32)$$

It is easy to find that its general solution is given by

$$\boldsymbol{F}_k(t,t_0)=iV_k\int_{t_0}^{t}\boldsymbol{U}(\tau,t_0)\begin{pmatrix}e^{-2i\epsilon_k\tau}&e^{2i\epsilon_k\tau}\\-e^{-2i\epsilon_k\tau}&-e^{2i\epsilon_k\tau}\end{pmatrix}d\tau,\quad(33)$$

which generates the nonequilibrium correlation Green function $\boldsymbol{V}(t,\tau)$:

$$\boldsymbol{V}(t,\tau)=\sum_k\langle\boldsymbol{F}_k^\dagger(\tau,t_0)\begin{pmatrix}b_k^\dagger(t_0)\\b_k(t_0)\end{pmatrix}(b_k(t_0)\;b_k^\dagger(t_0))\boldsymbol{F}_k(t,t_0)\rangle.\quad(34)$$

The nonequilibrium correlation Green function $\boldsymbol{V}(t,\tau)$ describes the particle-hole and particle-particle correlations arose from the fluctuations of the spin chain. Notice that if the flipping energy of the probing spin σ_0 equals zero ($\omega_0=0$), then as shown in our previous work [35], the nonequilibrium Green functions $\boldsymbol{U}(t,t_0)$ and $\boldsymbol{V}(\tau,t)$ obey the following identities

$$\begin{aligned}&\boldsymbol{U}_{11}(t,t_0)=\boldsymbol{U}_{22}(t,t_0),\;\boldsymbol{U}_{12}(t,t_0)=\boldsymbol{U}_{21}(t,t_0),\\&\boldsymbol{V}_{11}(\tau,t)=\boldsymbol{V}_{22}(\tau,t)=-\boldsymbol{V}_{12}(\tau,t)=-\boldsymbol{V}_{21}(\tau,t).\end{aligned}\quad(35a)$$

Thus, the time-dependent dissipation and fluctuation coefficients in the master equation Eq. (18) are reduced to

$$\gamma(t,t_0)=\tilde{\gamma}(t,t_0)=-\Lambda(t,t_0)=[\dot{\boldsymbol{U}}(t,t_0)\boldsymbol{U}^{-1}(t,t_0)]_{12},\quad(36)$$

that are solely determined by the retarded Green function $\boldsymbol{U}(t,t_0)$. As a consequence, the dynamics process will be independent of the initial state of the spin chain if $\omega_0=0$.

B. Decoherence dynamics for different phase of the spin chain

Through the relation between the time-dependent dissipation $\gamma(t,t_0)$, $\Lambda(t,t_0)$ and the fluctuation coefficients $\tilde{\gamma}(t,t_0)$ in the exact master equation and the nonequilibrium retarded and correlation Green functions, $\boldsymbol{U}(t,t_0)$ and $\boldsymbol{V}(t,\tau)$, we can analytically solve the non-Markovian dynamics of the probing spin σ_0, from which the topological dynamics of the spin chain can be manifested in the real-time domain. As we also discussed earlier, the spin chain undergoes a topological phase transition from the topologically nontrivial phase to the topologically trivial phase when λ changes across the critical point $\lambda_c=1$. To understand the manifestation of the topological phase transition in terms of the real-time non-Markovian decoherence dynamics of the probing spin σ_0, we study the two-time spin correlation

$$\begin{aligned}\left\langle\sigma_0^z(t)\sigma_0^z(t_0)\right\rangle=&\langle4a^\dagger(t)a(t)a^\dagger(t_0)a(t_0)\rangle-\langle2a^\dagger(t)a(t)\rangle\\&-\langle2a^\dagger(t_0)a(t_0)\rangle+1\end{aligned}\quad(37)$$

by varying the value of λ. For simplicity, we first set $\omega_0=0$ and $\eta=J$. The result of the correlation $\langle\sigma_0^z(t)\sigma_0^z(t_0)\rangle$ with different λ is shown in Fig. 4(a). Figure 4(a) shows clearly a critical transition at $\lambda=1$. The two-time correlation keeps oscillation between the positive and negative value in all the time for $\lambda<1$, while although it also oscillates for $\lambda>1$ in the beginning, it will eventually approach to a stationary value.

To understand the underlying mechanism of this transition, we plot the real part of the determinant of $\tilde{\boldsymbol{U}}^{-1}(s)$ with different λ in Fig. 4(b), which determines the localized modes of the probing spin. Notice that there are discontinuous parts (the flat lines) in the function due to the nonzero values of the imaginary part of $\tilde{\boldsymbol{U}}^{-1}(s)$ in these regions, and the imaginary part is determined by the spectral density $\mathcal{J}(s)$ in Eq. (24). The discontinuous parts locate exactly in the regions where the spectral density has nonzero value. As we have discussed earlier, the poles $\{s_p\}$ that make $|\tilde{\boldsymbol{U}}(s_p)|^{-1}=0$ form the localized modes and contribute the dissipationless term in Eq. (30). The locations of these poles are the intersection points of $\mathrm{Re}[|\tilde{\boldsymbol{U}}(s)|^{-1}]$ and the horizontal axis with the spectral density

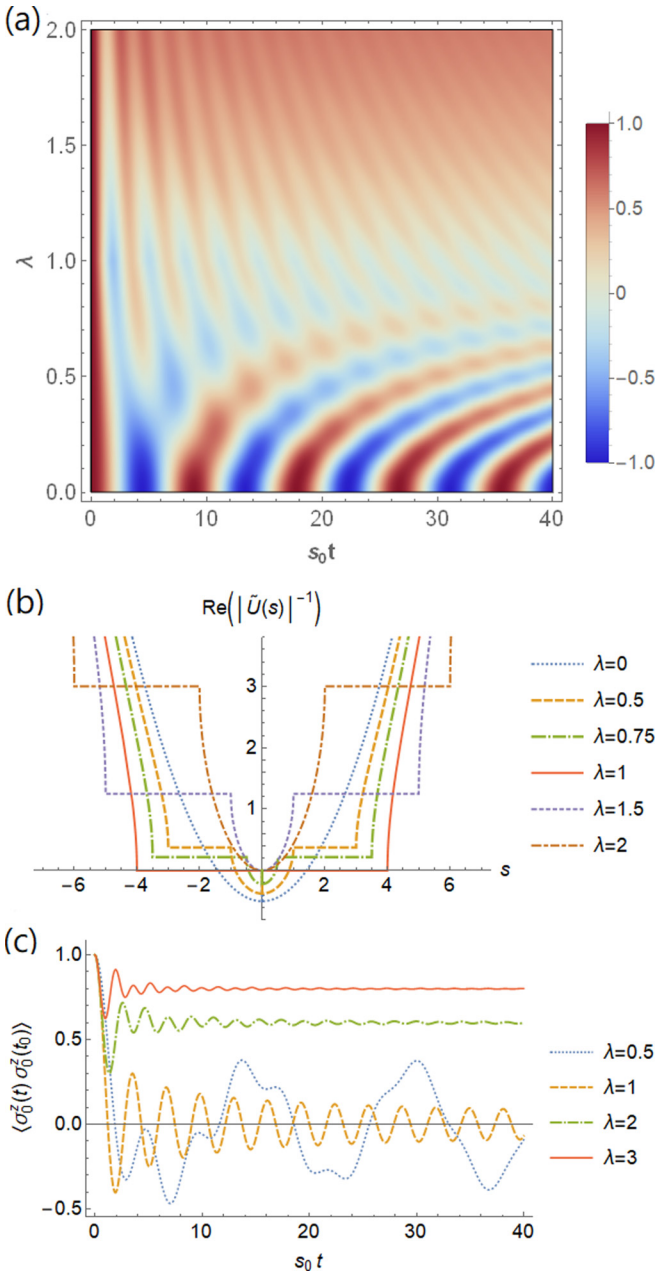

FIG. 4. (a) A contour plot of the two-time correlation $\langle\sigma_0^z(t)\sigma_0^z(t_0)\rangle$ by varying the time t and λ for $\eta = J$ and $\omega_0 = 0$, where $s_0 = 2J/\hbar$. (b) The inverse of the determinant of $\tilde{\boldsymbol{U}}(s)$ with different λ. (c) The two-time correlation $\langle\sigma_0^z(t)\sigma_0^z(t_0)\rangle$ with $\eta = J$ and $\omega_0 = 0$ for different values of λ.

$\mathcal{J}(s) = 0$ (the imaginary part of $|\tilde{\boldsymbol{U}}(s)|^{-1}$ vanishes). In other words, the different decoherence dynamics associated with the topological phase transition is determined by these different dissipationless-localized modes.

More specifically, we first consider the case of $\lambda = 0$ that the probing spin σ_0 is only coupled to the left Majorana zero mode because it perfectly locates at the left end of the spin chain, as we have shown in Sec. II. In this case, there are three localized modes [one pole located at 0 and two symmetrically located at the positive and negative sides, as shown in Fig. 4(b)]. Then the energy keeps exchange between the probing spin σ_0 and the zero-energy bogoliubon of the spin chain through the left Majorana zero mode. This leads to the two-time correlation as a cosinusoidal oscillation for $\lambda = 0$, as we can see in Fig. 4(a).

Once $\lambda > 0$, the probing spin σ_0 will couple to not only the left Majorana zero mode but also other modes with higher energy in the spin chain, so its energy will also dissipate to the nonzero continuous modes of the spin chain. This leads to a nonexponential decay given by the latter term in Eq. (30). In fact, in the topologically nontrivial phase ($\lambda < 1$), Fig. 4(b) shows that there are always three localized modes. Therefore, after a short-time decay, the two-time correlation will reduce to a dissipationless oscillation. As λ increasing, the decay term will become more and more dominant. When it reaches to the critical point $\lambda = 1$, all the localized modes vanish [see Fig. 4(b) and Fig. 3]. Thus, the dissipationless term vanishes in Eq. (30), and the spin correlation shows the maximum decoherence effect.

On the other hand, in the topologically trivial phase ($\lambda > 1$), Fig. 4(b) shows that only one localized mode occurs at $s_p = 0$. This leads to the two-time correlation eventually approaching a stationary value (no oscillation). Furthermore, if λ keeps increasing, the coupling term $\eta\sigma_0\sigma_1$ between the two subsystems in the total Hamiltonian becomes relatively weak, which results in the two subsystems being loosely affected to each other. As a result, we can see that the dynamics of the two-time correlation becomes more and more stable as λ gets larger and larger, as shown in Fig. 4(c).

C. Decoherence dynamics for different spin-spin chain coupling

Notice that the coupling η between the two subsystems can significantly affect the non-Markovian decoherence dynamics which is fully determined by the density of states of the spin chain and the coupling between the probing spin and the spin chain through the spectral density Eq. (24). In Figs. 5(a), 5(b), and 5(c), we plot the two-time correlation $\langle\sigma_0^z(t)\sigma_0^z(t_0)\rangle$ with different values of η for the topologically nontrivial phase ($\lambda = 0$), the critical point ($\lambda = 1$), and the topologically trivial phase ($\lambda = 2$), respectively. To understand these different behaviors of the correlations in different coupling regions, we plot again the real part of the determinant of $\tilde{\boldsymbol{U}}^{-1}(s)$ with the different corresponding values of η in Figs. 5(d), 5(e), and 5(f). Figure 5(d) shows that for the topologically nontrivial phase ($\lambda = 0$), there exist always three localized modes, which are independent of the value of η (except for the trivial case $\eta = 0$). The two-time correlation always shows a cosinusoidal oscillation. Figure 5(d) also shows that the change of η will affect the locations of the localized modes, which determine the frequencies of the dissipationless oscillation. Because the stronger the coupling η is, the easier it is to exchange energy between the two subsystems and the probing spin is affected from the topologically nonlocal state of the spin chain, the two-time correlation shows the oscillation with the higher frequency, as shown in Fig. 5(a).

At the critical point ($\lambda = 1$), Fig. 5(e) shows that when $\eta < J$, the real part of $|\tilde{\boldsymbol{U}}^{-1}|(s)$ vanishes only at $s = 0$ where the imaginary part has nonzero value [the spectral density $\mathcal{J}(0) > 0$, see Fig. 3]. Hence, there is no pole (localized

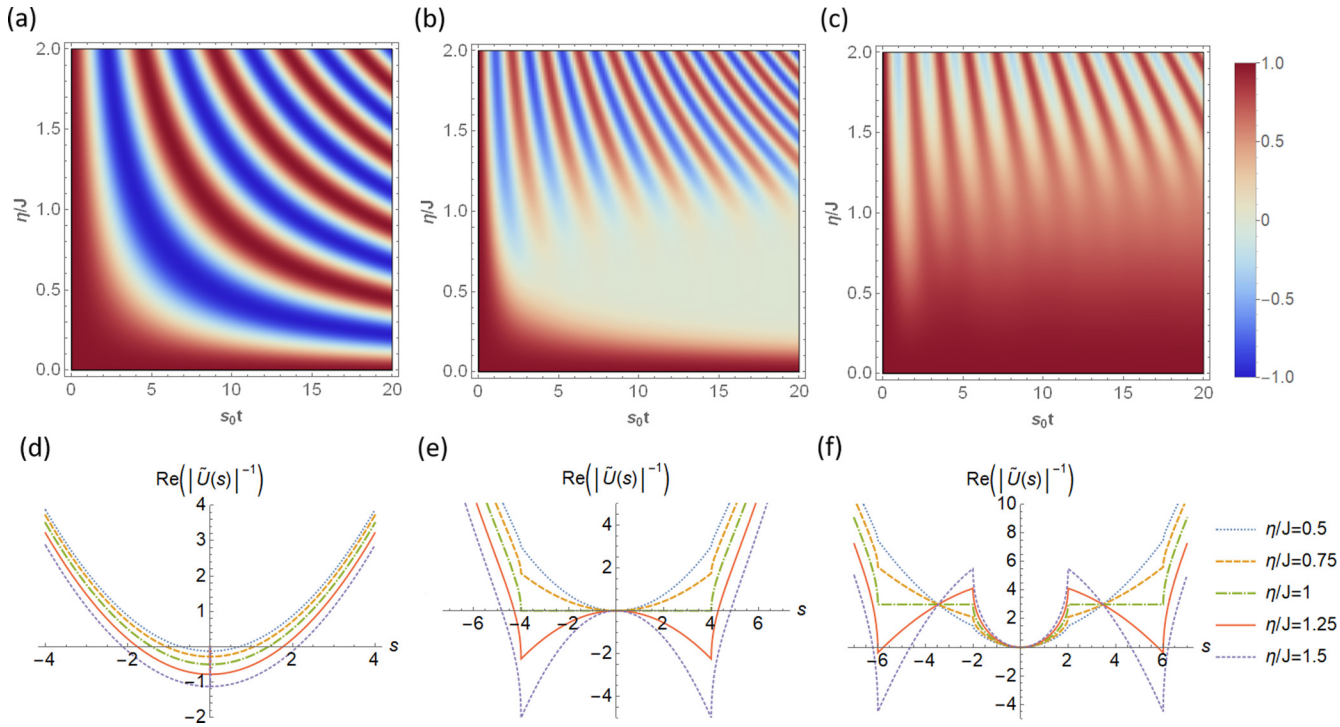

FIG. 5. The contour plot of the two-time spin-spin correlation $\langle\sigma_0^z(t)\sigma_0^z(t_0)\rangle$ by varying the time t and η/J for $\omega_0 = 0$ with (a) $\lambda = 0$, (b) $\lambda = 1$, and (c) $\lambda = 2$, respectively, and the inverse of the determinant of $\tilde{\boldsymbol{U}}(s)$ with different η for (d) $\lambda = 0$, (e) $\lambda = 1$, and (f) $\lambda = 2$, respectively.

mode) in this region, and the two-time correlation decays to zero monotonically, as a typical Markov process. On the other hand, we find from Fig. 5(e) that there are two localized modes when $\eta > J$, and thus the dissipationless oscillation terms get contribution in the two-time correlation. As a result, the dynamics of the probing spin σ_0 undergoes a transition from a Markovian process in the weak coupling region to a non-Markovian process in the strong coupling region, as shown in Fig. 5(b).

For the topologically trivial phase ($\lambda = 2$), Fig. 5(f) show that there is only one localized mode at $s = 0$ in the weak coupling region as we mentioned in Fig. 4. But there are three localized modes in the strong coupling region. Note that the intersection points located between $2 < |s| < 6$ in Fig. 5(f) are not poles because the imaginary part of $|\tilde{\boldsymbol{U}}^{-1}|(s)$ has nonzero value in this range, as shown in Fig. 3. In conclusion, the two subsystems exchange energy in the beginning in the weak coupling region ($\eta < J$), and then they reach the qualitatively different steady states for the different topological phases of the spin chain. When the coupling η between the two subsystems gets stronger, the probing spin has to take longer time to reach the steady state, while the two subsystems always maintain energy exchange in the both phases of the spin chain in the strong coupling region ($\eta > J$). Thus, the topological effect of the spin chain to the decoherence dynamics of the probing spin becomes insignificant.

D. Decoherence dynamics for different spin-flip energy

In the previous discussion, we only discuss about the case that the probing spin σ_0 has zero flipping energy ($\omega_0 = 0$), in which the time-dependent coefficients in the master equation are independent of the correlation Green function $\boldsymbol{V}(t,t)$, as shown in Eq. (34). In other words, for $\omega_0 = 0$, the decoherence dynamics is independent of the environmental noise which is associated with the initial state of the spin chain. To have a further understanding of the effect of the spin-flip energy ω_0 to the decoherence dynamics of the spin σ_0 and the consequence of the initial dependence of the spin chain, we first plot the real part of the determinant of $\tilde{\boldsymbol{U}}^{-1}(s)$ again for topologically nontrivial phase, topologically trivial phase, and critical point in different coupling regions with different values of ω_0 in Fig. 6. Figure 6 shows that the increase of ω_0 always makes the locations of the localized modes away from zero, which may affect the number of localized modes, as listed in Table I. For the localized modes numbers $a + b$ listed in Table I, a is the number of the localized modes located between $-2|1-\lambda| < s < 2|1-\lambda|$ and b is that in

TABLE I. The number of localized modes with different values of ω_0, η, and λ.

	$\lambda < 1$	$\lambda = 1$	$\lambda > 1$
$\eta \leqslant J, \omega_0 = 0$	3+0	0+0	1+0
$\eta \leqslant J, 0 < \omega_0 \leqslant \omega_1$	3+0	×	2+0
$\eta \leqslant J, \omega_1 < \omega_0 < \omega_2$	1+0	0+0	0+0
$\eta \leqslant J, \omega_2 \leqslant \omega_0$	1+2	0+2	0+2
$\eta > J, \omega_0 = 0$	3+2	0+2	1+2
$\eta > J, 0 < \omega_0 \leqslant \omega_1$	3+2	×	2+2
$\eta > J, \omega_1 < \omega_0$	1+2	0+2	0+2

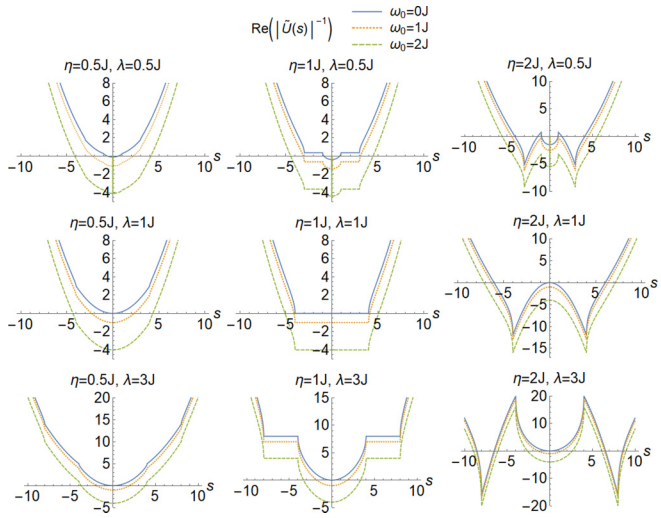

FIG. 6. The inverse of the determinant of $\tilde{\boldsymbol{U}}(s)$ with different values of ω_0 in both phases and different coupling regions.

$s < -2(1+\lambda)$ or $s > 2(1+\lambda)$. Notice that these numbers will change when ω_0 crosses ω_1 or ω_2, where

$$\omega_1 = \begin{cases} \sqrt{(1-\lambda)(1-\lambda-\eta^2(1-3\lambda)/2J^2)} & \lambda < 1 \\ \sqrt{(\lambda-1)(\lambda-1+2\eta^2/J^2)} & \lambda \geqslant 1 \end{cases} \tag{38a}$$

$$\omega_2 = \begin{cases} \sqrt{(1+\lambda)(1+\lambda-\eta^2(1+3\lambda)/2J^2)} & \lambda < 1 \\ \sqrt{(1+\lambda)(1+\lambda-2\eta^2/J^2)} & \lambda \geqslant 1 \end{cases}. \tag{38b}$$

For special case $\lambda = 1$, we have $\omega_1 = 0$, and for the case $\eta = J$, we have $\omega_1 = \omega_2$. Moreover, the amplitudes of the localized modes located in these two regions have contrast behavior as ω_0 increasing. The amplitudes of the localized modes decrease in the region $-2|1-\lambda| < s < 2|1-\lambda|$, while they increase in the region $s < -2(1+\lambda)$ or $s > 2(1+\lambda)$. This can be seen clearly from Fig. 7 where the summation of the amplitudes of all localized modes versus ω_0 is plotted.

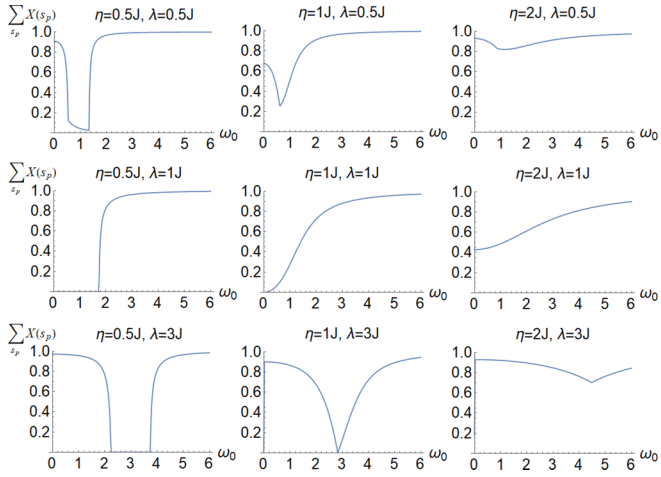

FIG. 7. The summation of the amplitudes of all localized modes versus ω_0 in each phase and coupling region.

Nevertheless, for $\omega_0 \neq 0$, the decoherence dynamics is no longer solely determined by the dissipation from $\boldsymbol{U}(t,t_0)$, but also the fluctuations associated with the initial states of both the probing spin σ_0 and the spin chain through the correlation Green function $\boldsymbol{V}(t,t)$. To obtain a more comprehensive physical picture, we plot the two-time correlation $\langle\sigma_0(t)\sigma_0(t_0)\rangle$ with different values of ω_0 and different initial states of σ_0 for the spin chain in the topologically nontrivial phase ($\lambda = 1/2$), the critical point ($\lambda = 1$), and the topologically trivial phase ($\lambda = 3$), see Figs. 8(a), 8(b), and 8(c), respectively. The results show that if the probing spin σ_0 is initially in the high-energy (spin-down) state, its energy will be dissipated into the spin chain, and it tends to decay to the low-energy (spin-up) state. If the probing spin σ_0 is initially in the low-energy state, it exchanges little energy with the spin chain and most likely remains in the low-energy state. The larger the value of ω_0 is, the more apparent this phenomenon can be seen in the region $\omega_0 < \omega_1$, where the localized modes are all located between $-2|1-\lambda| < s < 2|1-\lambda|$. However, for $\omega_0 > \omega_2$, the amplitudes of the localized modes become large with increasing ω_0, so that even if the probing spin is in the high-energy state, it becomes harder to dissipate its energy into the spin chain [see the dashed green lines in Fig. 8(a) and Fig. 8(b)].

Moreover, for $\omega_0 \neq 0$, the initial state of the spin chain also affects the decoherence dynamics of the probing spin σ_0. The spin chain is assumed initially in thermal equilibrium state. We plot again the two-time correlation for different phases with the spin chain at initial finite temperature $k_BT = 5J$ in Figs. 8(d), 8(e), and 8(f). The results show that for the high temperature, the two diagonal terms of the correlation Green function $\boldsymbol{V}_{11}(t,t)$ and $\boldsymbol{V}_{22}(t,t)$ are similar. As a result, the two-time correlations of the two initial states become closer to each other, as shown in Figs. 8(d), 8(e), and 8(f). In other words, if the spin chain is initially at a relatively high temperature, the dependence of the non-Markovian decoherence dynamics on the initial state of σ_0 will diminish because the thermal fluctuation dominates the non-Markovian decoherence dynamics.

Putting all the above analyses together, we find that all the parameters λ, η, and ω_0 can induce different number of the localized modes with different amplitudes and therefore affect differently the non-Markovian decoherence dynamics associated with the topological states. In particular, for $\omega_0 = 0$ and in the weak coupling region, the topological phase transition can be significantly manifested in the dissipation dynamics of the probing spin σ_0. In other words, the topological structure of the spin chain can be observed through the non-Markovian decoherence dynamics of the probing spin σ_0. On the other hand, in the strong coupling region, the topological nonlocal state is more strongly coupled to the probing spin so that the topological effect in the non-Markovian dynamics becomes more significant, as shown in Fig. 5. However, for $\omega_0 \neq 0$, the noise effect gets involved into the decoherence dynamics, which is strongly correlated with the initial state of spin σ_0 and the initial temperature of the spin chain. As a result, the manifestation of the topological structure of the spin chain on the non-Markovian decoherence dynamics of the probing spin σ_0 is merged. Hence, we propose the experimental probe of the topological structure of the spin chain through the

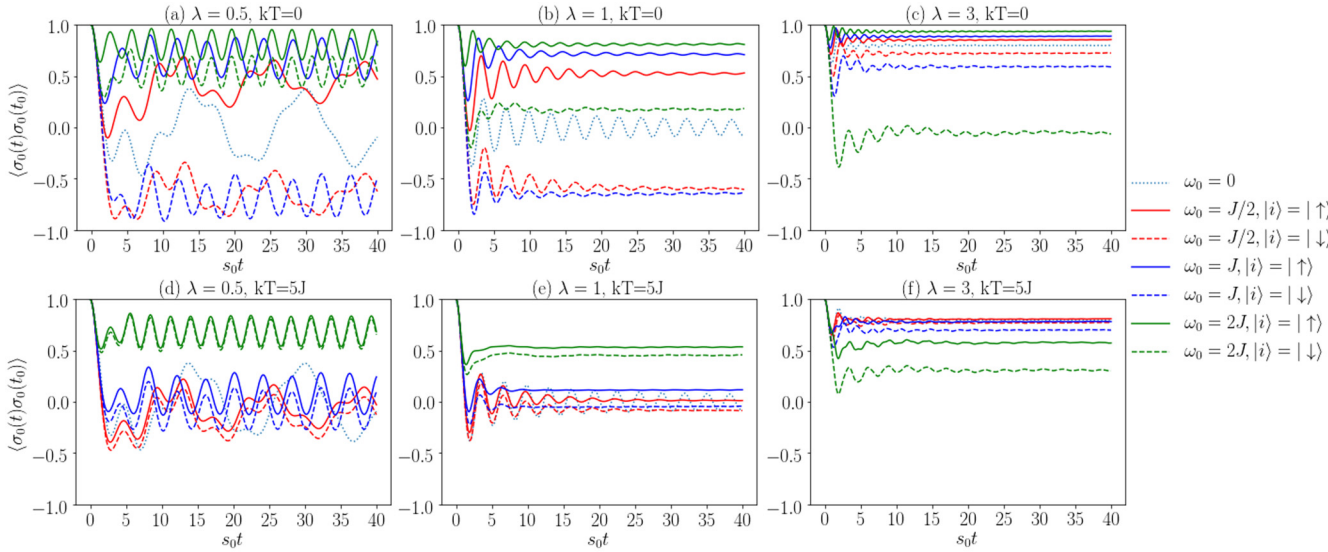

FIG. 8. The two-time correlation $\langle\sigma_0^z(t)\sigma_0^z(t_0)\rangle$ with different initial states of σ_0 and different values of ω_0 for (a) $\lambda = 1/2$, (b) $\lambda = 1$, (c) $\lambda = 3$ at zero temperature and for (d) $\lambda = 1/2$, (e) $\lambda = 1$, (f) $\lambda = 3$ at temperature $T = 5J/k_B$.

decoherence dynamics of an external spin σ_0 coupling *weakly* to the spin chain at low temperature.

V. THE DYNAMICS OF ENTANGLEMENT ENTROPY

In this section, we study the dynamics of the quantum entanglement. In the static case, the behavior of the entanglement has a universal character that the entanglement of the system state would be enhanced near a quantum phase transition and reach the maximum at the critical point. Therefore, it can be used as an estimator of quantum correlations [44] and as a detector to classify quantum phase transitions [10,36,39,45]. It is also interesting to see how entanglement developed in time when the system is far away from the equilibrium state or ground state. Therefore, we would like to further investigate the relation between the entanglement and quantum phase transitions in the nonequilibrium region.

The entanglement between the probing spin σ_0 and the spin chain can be characterized by the von Neumann entropy $S_A(t) = -\mathrm{Tr}[\rho_A(t)\ln\rho_A(t)]$. The reduced density matrix $\rho_A(t)$ of the probing spin σ_0 that obeys the master equation Eq. (18) can be expressed as

$$(\rho_A)_{11}(t) = \boldsymbol{V}_{22}(t,t) + \boldsymbol{U}_{12}(t,t_0)\boldsymbol{U}_{21}(t,t_0)\langle a^\dagger(t_0)a(t_0)\rangle + \boldsymbol{U}_{11}(t,t_0)\boldsymbol{U}_{22}(t,t_0)\langle a(t_0)a^\dagger(t_0)\rangle \tag{39a}$$

$$(\rho_A)_{22}(t) = \boldsymbol{V}_{11}(t,t) + \boldsymbol{U}_{11}(t,t_0)\boldsymbol{U}_{22}(t,t_0)\langle a^\dagger(t_0)a(t_0)\rangle + \boldsymbol{U}_{12}(t,t_0)\boldsymbol{U}_{21}(t,t_0)\langle a(t_0)a^\dagger(t_0)\rangle \tag{39b}$$

$$(\rho_A)_{12}(t) = (\rho_A)_{21}^*(t) = \boldsymbol{U}_{11}(t,t_0)\langle a(t_0)\rangle + \boldsymbol{U}_{12}(t,t_0)\langle a^\dagger(t_0)\rangle. \tag{39c}$$

Moreover, we find that there is a relation between the entanglement entropy $S_A(t)$ and the two-time correlation $\langle\sigma_0^z(t)\sigma_0^z(t_0)\rangle$ if the initial state of σ_0 is a pure state, which is given by

$$S_A(t) = -\frac{1-\langle\sigma_0^z(t)\sigma_0^z(t_0)\rangle}{2}\ln\frac{1-\langle\sigma_0^z(t)\sigma_0^z(t_0)\rangle}{2} - \frac{1+\langle\sigma_0^z(t)\sigma_0^z(t_0)\rangle}{2}\ln\frac{1+\langle\sigma_0^z(t)\sigma_0^z(t_0)\rangle}{2}. \tag{40}$$

We plot $S_A(t)$ for $\omega_0 = 0$ and $\eta = J$ with different values of λ in Fig. 9(a). In this case, we have $\boldsymbol{V}_{11}(t,t) = \boldsymbol{V}_{22}(t,t)$, then the entanglement entropy is independent of the initial state of the spin chain, as we mentioned in Sec. III. The probing spin σ_0 is assumed to be initially in a pure state. In the beginning, there is no entanglement between σ_0 and the spin chain, and the entropy $S_A(t_0)$ equals zero. When $t > t_0$, the probing spin σ_0 begins to entangle with the spin chain due to the coupling between them so that the entropy S_A increases from 0 in Fig. 9(a). For $\lambda < 1$, the entanglement entropy always keeps oscillating, which means that the probing spin σ_0 and the spin chain never reach the equilibrium state due to the existence of localized modes [31]. The maximum value of such entanglement entropy oscillation is always $\ln 2$, while its lower bound rises as λ increases. For $\lambda \geqslant 1$, the probing spin σ_0 will reach equilibrium with the spin chain in the long-time limit, and the entanglement entropy will approach to a stationary value which decreases as λ increases. Note that the entanglement entropy approaches to $\ln 2$ at $\lambda = 1$, in agreement with the expectation that there is maximum entanglement at the critical point of topological phase transitions. We further plot the entanglement entropy versus λ under the long-time limit in Fig. 9(b) to see more clearly its close relation with topological phase transition. Figure 9(b) shows a qualitative change of the entanglement entropy when the topological phase transition occurs. It shows that the entanglement entropy can be used to diagnose topological phase transitions in the nonequilibrium regions.

However, for the case of $\omega_0 \neq 0$, the entanglement entropy also depends on the initial states of both the probing spin σ_0

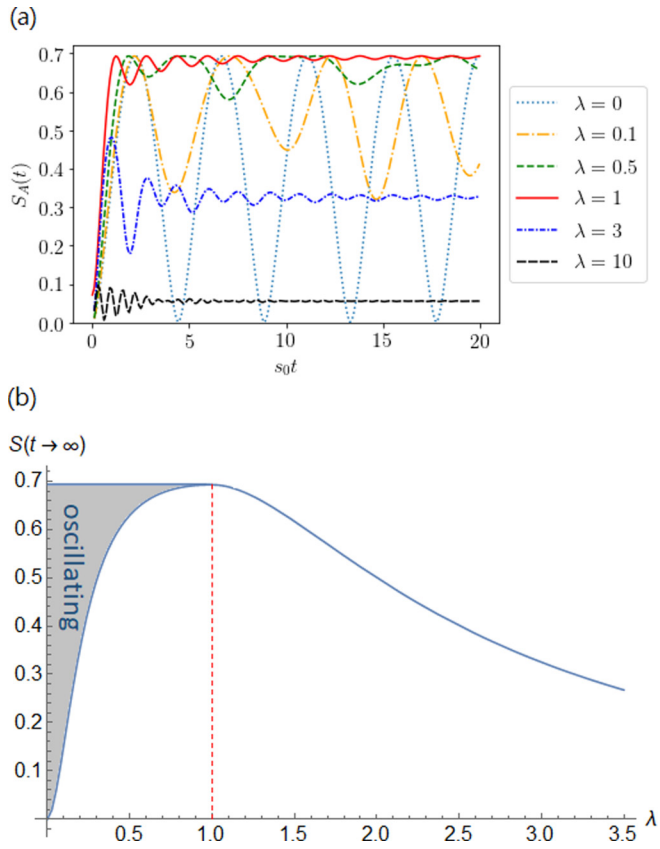

FIG. 9. (a) The entanglement entropy $S_A(t)$ for $\omega_0 = 0$ and $\eta = J$ with the spin chain varying from the topologically nontrivial phase ($\lambda < 1$) to the topologically trivial phase ($\lambda > 1$). (b) The long-time entanglement entropy versus λ.

and the spin chain. The entanglement entropy $S_A(t)$ for the spin chain with the zero initial temperature in topologically nontrivial phase $\lambda < 1$, critical point $\lambda = 1$, and topologically trivial phase $\lambda > 1$ is presented in Figs. 10(a), 10(b), and 10(c), respectively. The results show that the different initial states of the probing spin σ_0 induce very different behaviors of the entanglement entropy, particularly for the high spin-flip energy ω_0. This is because the probing spin σ_0 with the high-energy initial state is more favored to decay than that with the low-energy initial state. For a small value of ω_0, the probing spin σ_0 initially in the low-energy state tends to remain in the pure initial state, while σ_0 which is initially in the high-energy state tends to decay to the mixed state. As a result, we can see in Fig. 10 that for $\omega_0 = 0.5J$ (red lines) and $\omega_0 = 2J$ (green lines), the probing spin σ_0 with the low-energy initial state $|\uparrow\rangle$ is less favored to be entangled with the spin chain, while the probing spin σ_0 with the high-energy initial state $|\downarrow\rangle$ is more favored to entangle with the spin chain.

On the other hand, for a larger value of ω_0, the probing spin σ_0 initially in the low-energy state still remains in its initial state, while the spin initially in the high-energy state tends to decay to the low-energy state. In both cases, the probing spin σ_0 tends to evolve toward the pure state so that the probing spin σ_0 and the spin chain are less entangled, as we can see from the result of $\omega_0 = 5J$ (yellow line) in Fig. 10. More importantly, we can see in Fig. 10 that for $\omega_0 \neq 0$, the critical point does not always has the maximum entanglement, i.e., the enhancement of the entanglement near the critical region is suppressed in this case. We also plot the entanglement entropy in different phases with the initial temperature of the spin chain $k_BT = 5J$ in Figs. 10(d), 10(e), and 10(f). The results show that the dependence of the initial state of σ_0 also diminish in the high temperature due to the thermal fluctuation. Meanwhile, the thermal fluctuation makes the entanglement entropy increase, particularly for the high-energy initial state $|\downarrow\rangle$ of σ_0. These results for $\omega_0 \neq 0$ show that the relation between the entanglement entropy and topological phase transition is less obvious due to the initial state dependence and the thermal effect. Therefore, we find again

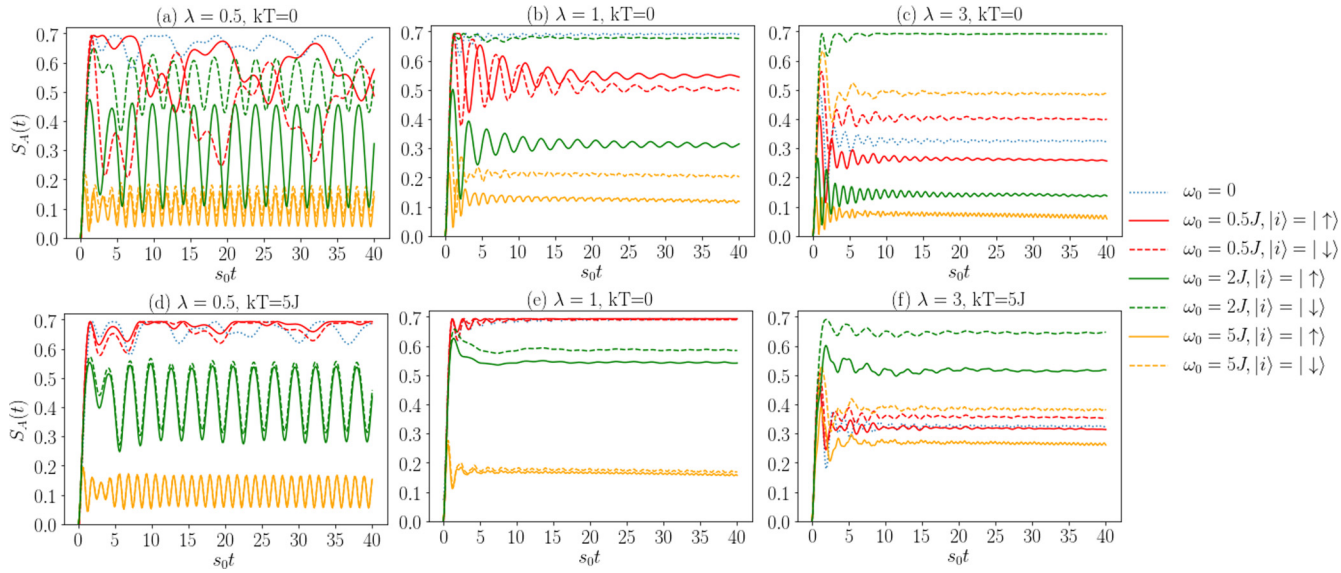

FIG. 10. The entanglement entropy S_A with different initial states of σ_0 and different values of ω_0 for (a) $\lambda = 1/2$, (b) $\lambda = 1$, (c) $\lambda = 3$ in zero temperature and for (d) $\lambda = 1/2$, (e) $\lambda = 1$, (f) $\lambda = 3$ in temperature $T = 5J/k_B$.

that to properly probe the relation between the entanglement and topological phase transitions through the probing spin, it is crucial to control the flip energy of the probing spin σ_0 small and make the spin chain at low temperature.

VI. CONCLUSION AND PERSPECTIVE

The energy eigenfunctions of the conventional transverse-field Ising model, or the equivalent Kitaev model, cannot be analytically solved with the free-end boundary condition even though in principle it is exactly solvable. We introduce a modified transverse-field Ising chain with zero local transverse field at the last site of the spin chain ($h_N = 0$) such that the model becomes analytically solvable. Its spectrum as well as its ground state wave-function distribution with those of the ordinary transverse-field Ising model are comparable but are also distinguishable. We show that different from the ground states of the original spin model which has zero energy only for $\lambda < 1$ for large N, the twofold degenerate zero energy ground states (zero modes) always exists in the modified transverse-field Ising model for all the values of λ, but the modified model still has the topological phase transition at $\lambda = 1$, namely the zero energy ground state wave functions have different topological properties for $\lambda < 1$ and $\lambda > 1$, which cannot be seen obviously in its spectrum. We also prove that the phase transition is associated with the change of the topological winding number of the ground state wave functions. Moreover, in the modified model, the results of the ground state wave-function distributions indicate that the right Majorana zero mode is always located at the right end of the spin chain because $h_N = 0$. The distribution of the left Majorana zero mode is the same as that of the ordinary model for $\lambda < 1$ so that the two Majorana zero modes are nonlocally separated (topologically nontrivial). While for $\lambda > 1$ the left Majorana zero mode in the modified model moves to the right-hand side and eventually merges with the right Majorana zero mode such that the zero energy Majorana modes become topologically trivial.

We then propose a scheme to measure the topological structure of the modified spin chain through the non-Markovian decoherence dynamics of a probing spin in the real-time domain by coupling the probing spin to the spin chain. We derive the exact master equation of a probing spin and analyzed in detail its non-Markovian decoherence dynamics by studying the two-time correlation function $\langle\sigma_0^z(t)\sigma_0^z(t_0)\rangle$. We find that:

(i) In the topologically nontrivial phase, the topological nonlocal property induces different localized modes in comparison with the case in the topologically trivial phase. These localized modes qualitatively change the non-Markovian decoherence dynamics of the probing spin so that the topological structure of the transverse-field Ising chain is manifested.

(ii) The coupling η between the probing spin and the spin chain, and the flipping energy ω_0 of the probing spin, also affect the non-Markovian decoherence dynamics. For strong coupling η, the non-Markovian oscillation is dominant in both phases so that the manifestation of the topological phase transition in the non-Markovian decoherence dynamics of the probing spin becomes weak. While for large spin-flip energy ω_0, the manifestation of topological and nontopological phases is also suppressed due to the noise effects associated with the initial state of the probing spin and the temperature of the spin chain.

(iii) The dynamical entanglement entropy can be expressed in the two-time correlation $\langle\sigma_0^z(t)\sigma_0^z(t_0)\rangle$ so that the entanglement entropy between the probing spin and the spin chain can characterize the topological phase transition, which is equivalent to the description of the decoherence dynamics of the probing spin, but the later may be more feasible for experimental realization.

As a result, the topological properties of the transverse-field Ising model can be probed through the non-Markovian decoherence dynamics of a probing spin weakly coupling to it, and the dynamical phase transition can be also explored in terms of the dynamical entanglement entropy, as long as one keeps the probing spin with a small spin-flip energy and the spin chain at a low temperature.

The results presented in this work provide indeed a general way to experimentally measure topological properties and dynamical phase transitions in many-body systems in the real-time domain, The decoherence properties of the probing spin can manifest the topological structure and dynamical phase transition of a many-body system because the decoherence dynamics of the probing particle is fully determined by the spectral density $J(\omega) = 2\pi\rho(\omega)|V(\omega)|^2$ which contains all information of the many-body spectra and many-body eigenfunction distributions through the density of state $\rho(\omega)$ and the coupling amplitude $V(\omega)$ between the probing spin and the many-body system. Current measurement of topological states are mainly carried out using surface-sensitive angle-resolved photoemission spectroscopy (ARPES) for directly observing surface states or the scanning tunneling microscope (STM) to visualize surface states in terms of the quasiparticle interference pattern in the energy domain. The decoherence dynamics of the probing spin can be experimentally measured with the time-domain single-spin Ramsey interferometry or spin echo technique. Furthermore, controllable coupling between the probing spin and many-body systems also serves as an alternative realization of the dynamical quench for the study of nonequilibrium dynamics of many-body systems, in particular the dynamical quantum phase transition. Therefore, one can measure topological properties and dynamical phase transitions in many-body systems in the real-time domain, in terms of single probing particle measurement, which should be more flexible in comparison with real-time many-body measurements.

ACKNOWLEDGMENT

We acknowledges the support from the Ministry of Science and Technology of Taiwan under Contract No. MOST-108-2112-M-006-009-MY3.

APPENDIX A

We rewrite the Hamiltonian of the transverse-field Ising chain with an arbitrary magnetic field at the last site ($h_N = h'$)

in the matrix form

$$H_B = \sum_{i,j=1}^{N} (c_i^\dagger A_{ij} c_j + c_i^\dagger B_{ij} c_j^\dagger + \text{H.c.}), \tag{A1}$$

where $A_{ii} = -h$, $A_{ii+1} = A_{i+1i} = B_{ii+1} = -B_{i+1i} = -J/2$ for $i < N$, $A_{NN} = h'$ and all others are zero. If Eq. (5) holds, then we have

$$[b_k, H_B] = \epsilon_k b_k, \tag{A2}$$

which gives

$$\epsilon_k u_{ki} = \sum_{j=1}^{N} (u_{kj} A_{ji} - v_{kj} B_{ji})$$

$$\epsilon_k v_{ki} = \sum_{j=1}^{N} (u_{kj} B_{ji} - v_{kj} A_{ji}). \tag{A3}$$

By introducing $(\Phi_k)_i = u_{ki} + v_{ki}$ and $(\Psi_k)_i = u_{ki} - v_{ki}$, Eq. (A3) can be simplified as

$$\Phi_k (A - B) = \epsilon_k \Psi_k$$

$$\Psi_k (A + B) = \epsilon_k \Phi_k \tag{A4}$$

$$\Rightarrow \begin{cases} \Phi_k (A - B)(A + B) = \epsilon_k^2 \Phi_k \\ \Psi_k (A + B)(A - B) = \epsilon_k^2 \Psi_k \end{cases}, \tag{A5}$$

where the relevant matrices

$$(A + B)(A - B) = J^2 \begin{bmatrix} \lambda^2 + 1 & \lambda & 0 & \cdots & 0 & 0 \\ \lambda & \lambda^2 + 1 & \lambda & \cdots & 0 & 0 \\ 0 & \lambda & \lambda^2 + 1 & \cdots & 0 & 0 \\ \vdots & \vdots & \vdots & \ddots & \vdots & \vdots \\ 0 & 0 & 0 & \cdots & \lambda^2 + 1 & \lambda' \\ 0 & 0 & 0 & \cdots & \lambda' & \lambda'^2 \end{bmatrix} \tag{A6a}$$

and

$$(A - B)(A + B) = J^2 \begin{bmatrix} \lambda^2 & \lambda & 0 & \cdots & 0 & 0 \\ \lambda & \lambda^2 + 1 & \lambda & \cdots & 0 & 0 \\ 0 & \lambda & \lambda^2 + 1 & \cdots & 0 & 0 \\ \vdots & \vdots & \vdots & \ddots & \vdots & \vdots \\ 0 & 0 & 0 & \cdots & \lambda^2 + 1 & \lambda \\ 0 & 0 & 0 & \cdots & \lambda & \lambda'^2 + 1 \end{bmatrix}. \tag{A6b}$$

These matrices have the eigenenergies

$$\epsilon_q^2 = J^2 (1 + \lambda^2 - 2\lambda \cos q), \tag{A7}$$

where all the normal modes q are determined by the following transcendental equation,

$$-\lambda' \sin[q(N-1)] = (1 + \lambda^2 - 2\lambda \cos q - \lambda'^2) \sin(Nq). \tag{A8}$$

Specifically, we have the following solutions:

(i) For the case $\lambda' = \lambda$, Eq. (A8) can be reduced to

$$\sin(qN) = \lambda \sin[q(N+1)], \tag{A9}$$

which determines all the normal modes q. For $\lambda \geqslant 1$, there are N real roots, exhausting the normal modes. For $\lambda < 1$, there are $N-1$ real roots and one imaginary root, as shown in Refs. [1,2].

(ii) In our case $\lambda' = 0$ (the modified model), Eq. (A8) is simply reduced to

$$(1 + \lambda^2 - 2\lambda \cos q) \sin(qN) = 0, \tag{A10}$$

which gives a set of $N-1$ solutions for $\sin(qN) = 0$, i.e.,

$$q_k = \frac{k\pi}{N}, \quad k = 1, 2, \ldots, N-1 \tag{A11}$$

and a special solution corresponding to the zero eigenvalue determined by

$$(1 + \lambda^2 - 2\lambda \cos q_0) = 0 \tag{A12}$$

for arbitrary λ value.

(iii) Note that this solution is also different from the transverse-field Ising model with period boundary condition. For the period boundary condition, we have the additional matrix element $A_{1N} = A_{N1} = B_{1N} = -B_{N1} = -J/2$. Then, the eigenenergies are still given by Eq. (A7) but the normal modes are simply determined by

$$\sin \frac{qN}{2} = 0. \tag{A13}$$

This gives all the N normal modes:

$$q_k = \frac{2\pi k}{N}, \quad k = 0, 1, 2, \ldots, N-1, \tag{A14}$$

in which the zero energy mode corresponds to $k = 0$ only for $\lambda = 1$. For other $\lambda \neq 1$, $\epsilon_k \neq 0$ for $k = 0$. It shows that the zero energy mode in three different cases are very different.

Now we focus on our modified model ($h_N = 0$). For $\epsilon_k \neq 0$, Ψ_k and Φ_k can be solved, respectively, from the two matrices by Eq. (A5)

$$(\Psi_k)_j = \alpha_k \sin \frac{jk\pi}{N} \tag{A15a}$$

$$(\Phi_k)_j = -\beta_k \frac{J}{\epsilon_k} \left\{ \sin \left[\frac{(j-1)k\pi}{N} \right] + \lambda \sin \frac{jk\pi}{N} \right\}, \tag{A15b}$$

and then we can obtain the wave functions for the nonzero-energy bogoliubons $u_{kj} = [(\Phi_k)_j + (\Psi_k)_j]/2$ and $v_{kj} = [(\Phi_k)_j - (\Psi_k)_j]/2$, shown as Eq. (7). The two constants α_k and β_k are determined by Eq. (A4) and the commutation relation $\{b_k, b_k^\dagger\} = 1$, and the result is $\alpha_k = \beta_k = 2\mathcal{N}_k$, where $\mathcal{N}_k$ is shown in Eq. (9a).

For $\epsilon = 0$, the eigenvectors of the two matrices are

$$\left(\Psi_{k_0}\right)_j = \alpha_0 \delta_{j,N} \tag{A16a}$$

$$\left(\Phi_{k_0}\right)_j = \beta_0 (-\lambda)^{j-1}. \tag{A16b}$$

The two constants α_0 and β_0 are determined by the commutation relations $\{b_0, b_0^\dagger\} = 1$ and $\{b_0, b_0\} = \{b_0^\dagger, b_0^\dagger\} = 0$ which

yield

$$\frac{1}{2}\sum_{j=1}^{N}\left[\left(\Phi_{k_0}\right)_j^2+\left(\Psi_{k_0}\right)_j^2\right]=1$$

$$\frac{1}{2}\sum_{j=1}^{N}\left[\left(\Phi_{k_0}\right)_j^2-\left(\Psi_{k_0}\right)_j^2\right]=0, \tag{A17}$$

and the results are $\alpha_0=1$ and $\beta_0=2\mathcal{N}_{k_0}$, where $\mathcal{N}_{k_0}$ is shown in Eq. (9b). Thus it is easy to obtain the wave function for the zero-energy bogoliubon $u_{k_0 j}$ and $v_{k_0 j}$, shown as Eq. (8).

APPENDIX B

We begin with Eq. (17) to derive the master equation. After integrating over all the degrees of freedom of the spin chain by path integral approach, we obtain the exact form of the propagating function

$$\begin{aligned}\mathcal{K}(\xi_f^*,\xi_f',t|\xi_0,\xi_0'^*,t_0)=\mathcal{N}(t)\exp\Bigg[&(\xi_f^*\quad \xi_f')\boldsymbol{J}_1(t,t_0)\begin{pmatrix}\xi_0\\ \xi_0'^*\end{pmatrix}\\&+(\xi_f^*\quad \xi_f')\boldsymbol{J}_2(t,t_0)\begin{pmatrix}\xi_f'\\ \xi_f^*\end{pmatrix}\\&+(\xi_0'^*\quad \xi_0)\boldsymbol{J}_3(t,t_0)\begin{pmatrix}\xi_0\\ \xi_0'^*\end{pmatrix}\\&+(\xi_0'^*\quad \xi_0)\boldsymbol{J}_1^\dagger(t,t_0)\begin{pmatrix}\xi_f'\\ \xi_f'^*\end{pmatrix}\Bigg],\end{aligned} \tag{B1}$$

where $\mathcal{N}(t)$ is the normalization constant and $\boldsymbol{J}_1(t,t_0)$, $\boldsymbol{J}_2(t,t_0)$, and $\boldsymbol{J}_3(t,t_0)$ are functions of the $\boldsymbol{U}(t,t_0)$ and $\boldsymbol{V}(t,t)$, and their exact formulas are given in Ref. [35].

After substituting Eq. (B1) into Eq. (17) and taking the time derivative on both sides, we have

$$\begin{aligned}\langle\xi_f|\dot\rho_A(t)|\xi_f'\rangle=\mathcal{N}(t)\int d\mu(\xi_0)d\mu(\xi_0')\langle\xi_0|\rho_A|\xi_0'\rangle&\\ \times\ \mathcal{K}(\xi_f^*,\xi_f',t|\xi_0,\xi_0'^*,t_0)&\\ \times\Bigg[\frac{\dot{\mathcal{N}}(t)}{\mathcal{N}(t)}+(\xi_f^*\quad \xi_f')\dot{\boldsymbol{J}}_1(t,t_0)\begin{pmatrix}\xi_0\\ \xi_0'^*\end{pmatrix}&\\ +(\xi_f^*\quad \xi_f')\dot{\boldsymbol{J}}_2(t,t_0)\begin{pmatrix}\xi_f'\\ \xi_f^*\end{pmatrix}+(\xi_0'^*\quad \xi_0)\dot{\boldsymbol{J}}_3(t,t_0)&\\ \times\begin{pmatrix}\xi_0\\ \xi_0'^*\end{pmatrix}+(\xi_0'^*\quad \xi_0)\dot{\boldsymbol{J}}_1^\dagger(t,t_0)\begin{pmatrix}\xi_f'\\ \xi_f'^*\end{pmatrix}\Bigg].&\end{aligned} \tag{B2}$$

The propagator $\mathcal{K}(\xi_f^*,\xi_f',t|\xi_0,\xi_0'^*,t_0)$ acting on the Grassmann numbers $\xi_0'^*$, ξ_0 of the initial state can be transferred into functions which only depend on the Grassmann numbers ξ_f', ξ_f^* of the state at time t. Then Eq. (B2) becomes

$$\begin{aligned}\langle\xi_f|\dot\rho_A(t)|\xi_f'\rangle=\langle\xi_f|\rho_A(t)|\xi_f'\rangle\Bigg[&\frac{\dot{\mathcal{N}}(t)}{\mathcal{N}(t)}+A(t)+B(t)\xi_f^*\xi_f'\\&+C(t)\xi_f^*\frac{\partial}{\partial\xi_f'}+D(t)\xi_f^*\frac{\partial}{\partial\xi_f^*}+E(t)\xi_f'\frac{\partial}{\partial\xi_f'}\\&+F(t)\xi_f'\frac{\partial}{\partial\xi_f^*}+G(t)\frac{\partial}{\partial\xi_f^*}\frac{\partial}{\partial\xi_f'}\Bigg],\end{aligned} \tag{B3}$$

where

$$A=\frac{\dot\mu_3(\nu_2)^2}{|\mu_1|^2-|\nu_1|^2} \tag{B4a}$$

$$B=\frac{2\nu_2(-\dot\mu_1\mu_1^*+\dot\nu_1\nu_1^*)-\dot\nu_3(\nu_2)^2}{|\mu_1|^2-|\nu_1|^2}+\dot\nu_2 \tag{B4b}$$

$$C=-F^*=\frac{-\dot\nu_1\mu_1+\dot\mu_1\nu_1}{|\mu_1|^2-|\nu_1|^2} \tag{B4c}$$

$$D=E=\frac{\dot\mu_1\mu_1^*-\dot\nu_1\nu_1^*+\dot\nu_3\nu_2}{|\mu_1|^2-|\nu_1|^2} \tag{B4d}$$

$$G=\frac{-\dot\nu_3}{|\mu_1|^2-|\nu_1|^2} \tag{B4e}$$

and

$$\nu_i(t,t_0)=[\boldsymbol{J}_i(t,t_0)]_{11}-[\boldsymbol{J}_i^\dagger(t,t_0)]_{22} \tag{B5a}$$

$$\mu_i(t,t_0)=[\boldsymbol{J}_i(t,t_0)]_{12}-[\boldsymbol{J}_i(t,t_0)]_{21}. \tag{B5b}$$

According to the three constraints: $\mathrm{Tr}\,\rho_A=1$, $a^\dagger a^\dagger=aa=0$, and the eigenenergies of A are symmetric in sign, Eq. (B4) can be reduced to

$$A=-\frac{\dot{\mathcal{N}}(t)}{\mathcal{N}(t)} \tag{B6}$$

$$B=\dot{\boldsymbol{V}}_{11}(t)-[\dot{\boldsymbol{U}}(t,t_0)\boldsymbol{U}^{-1}(t,t_0)\boldsymbol{V}(t,t)+\mathrm{H.c.}]_{11} \tag{B7}$$

$$C=-F^*=[\dot{\boldsymbol{U}}(t,t_0)\boldsymbol{U}^{-1}(t,t_0)]_{12} \tag{B8}$$

$$\begin{aligned}D=E=\dot{\boldsymbol{V}}_{11}(t)-[\dot{\boldsymbol{U}}(t,t_0)\boldsymbol{U}^{-1}(t,t_0)\boldsymbol{V}(t,t)+\mathrm{H.c.}]_{11}&\\ +[\boldsymbol{U}^{-1}(t,t_0)\dot{\boldsymbol{U}}(t,t_0)]_{11}^\dagger&\end{aligned} \tag{B9}$$

$$G=\dot{\boldsymbol{V}}_{11}(t)-[\dot{\boldsymbol{U}}(t,t_0)\boldsymbol{U}^{-1}(t,t_0)(\boldsymbol{V}(t,t)+\boldsymbol{I})+\mathrm{H.c.}]_{11}. \tag{B10}$$

Then using the D algebra of the creation and annihilation operators, we obtain the exact master equation

$$\begin{aligned}\dot\rho_A(t)=&-i[\epsilon(t)a^\dagger a,\rho_A(t)]\\&+\gamma(t)[2a\rho_A(t)a^\dagger-a^\dagger a\rho_A(t)-\rho_A(t)a^\dagger a]\\&+\tilde\gamma(t)[a^\dagger\rho_A(t)\sigma_0^- -a\rho_A(t)a^\dagger+a^\dagger a\rho_A(t)\\&-\rho_A(t)aa^\dagger]+\Lambda(t)a^\dagger\rho_A(t)a^\dagger+\Lambda^*(t)a\rho_A(t)a.\end{aligned} \tag{B11}$$

The time-dependent dissipation and fluctuation coefficients in the master equation are

$$\begin{aligned}\epsilon(t)&=i\left[D(t)-\frac{B(t)+G(t)}{2}\right]\\&=\frac{i}{2}[\dot{\boldsymbol{U}}(t,t_0)\boldsymbol{U}^{-1}(t,t_0)-\mathrm{H.c.}]_{11}.\end{aligned} \tag{B12a}$$

$$\begin{aligned}\gamma(t)&=\frac{G(t)-B(t)}{2}\\&=-\frac{1}{2}[\dot{\boldsymbol{U}}(t,t_0)\boldsymbol{U}^{-1}(t,t_0)+\mathrm{H.c.}]_{11},\end{aligned} \tag{B12b}$$

$$\tilde{\gamma}(t) = B(t) = \dot{\boldsymbol{V}}_{11}(t) - [\dot{\boldsymbol{U}}(t,t_0)\boldsymbol{U}^{-1}(t,t_0)\boldsymbol{V}(t,t) + \text{H.c.}]_{11}, \tag{B12c}$$

$$\Lambda(t) = -C(t) = -[\dot{\boldsymbol{U}}(t,t_0)\boldsymbol{U}^{-1}(t,t_0)]_{12}. \tag{B12d}$$

[1] E. Lieb, T. Schultz, and D. Mattis, Two soluble models of an antiferromagnetic chain, Ann. Phys. **16**, 407 (1961).

[2] P. Pfeuty, The one-dimensional Ising model with a transverse field, Ann. Phys. **57**, 79 (1970).

[3] R. Coldea, D. A. Tennant, E. M. Wheeler, E. Wawrzynska, D. Prabhakaran, M. Telling, K. Habicht, P. Smeibidl, and K. Kiefer, Quantum criticality in an Ising chain: Experimental evidence for emergent E8 symmetry, Science **327**, 177 (2010).

[4] A. Friedenauer, H. Schmitz, J. T. Glueckert, D. Porras, and T. Schaetz, Simulating a quantum magnet with trapped ions, Nat. Phys. **4**, 757 (2008).

[5] K. Kim, M. S. Chang, S. Korenblit, R. Islam, E. E. Edwards, J. K. Freericks, G. D. Lin, L. M. Duan, and C. Monroe, Quantum simulation of frustrated Ising spins with trapped ions, Nature (London) **465**, 590 (2010).

[6] R. Islam, E. E. Edwards, K. Kim, S. Korenblit, C. Noh, H. Carmichael, G.-D. Lin, L.-M. Duan, C. C. J. Wang, J. K. Freericks, and C. Monroe, Onset of a quantum phase transition with a trapped ion quantum simulator, Nat. Commun. **2**, 377 (2011).

[7] P. Jurcevic, H. Shen, P. Hauke, C. Maier, T. Brydges, C. Hempel, B. P. Lanyon, M. Heyl, R. Blatt, and C. F. Roos, Direct Observation of Dynamical Quantum Phase Transitions in An Interacting Many-Body System, Phys. Rev. Lett. **119**, 080501 (2017).

[8] J. Simon, W. S. Bakr, R. Ma, M. E. Tai, P. M. Preiss, and M. Greiner, Quantum simulation of antiferromagnetic spin chains in an optical lattice, Nature (London) **472**, 307 (2011).

[9] H. Labuhn, D. Barredo, S. Ravets, S. de Léséleuc, T. Macrì, T. Lahaye, and A. Browaeys, Tunable two-dimensional arrays of single Rydberg atoms for realizing quantum Ising models, Nature (London) **534**, 667 (2016).

[10] P. Calabrese and J. Cardy, Evolution of entanglement entropy in one-dimensional systems, J. Stat. Mech. (2005) P04010.

[11] P. Calabrese, F. H. L. Essler, and M. Fagotti, Quantum Quench in the Transverse-Field Ising Chain, Phys. Rev. Lett. **106**, 227203 (2011).

[12] M. Heyl, A. Polkovnikov, and S. Kehrein, Dynamical Quantum Phase Transitions in the Transverse-Field Ising Model, Phys. Rev. Lett. **110**, 135704 (2013).

[13] T. Puskarov and D. Schuricht, Time evolution during and after finite-time quantum quenches in the transverse-field Ising chain, SciPost Phys. **1**, 003 (2016).

[14] H. T. Quan, Z. Song, X. F. Liu, P. Zanardi, and C. P. Sun, Decay of Loschmidt Echo Enhanced by Quantum Criticality, Phys. Rev. Lett. **96**, 140604 (2006).

[15] P. Haikka, J. Goold, S. McEndoo, F. Plastina, and S. Maniscalco, Non-Markovianity, Loschmidt echo, and criticality: A unified picture, Phys. Rev. A **85**, 060101 (2012).

[16] F. J. Liu, X. X. Zhou, and Z. W. Zhou, Memory effect and non-Markovian dynamics in an open quantum system, Phys. Rev. A **99**, 052119 (2019).

[17] H. Weisbrich, C. Saussol, W. Belzig, and G. Rastelli, Decoherence in the quantum Ising model with transverse dissipative interaction in the strong-coupling regime, Phys. Rev. A **98**, 052109 (2018).

[18] H. Weisbrich, W. Belzig, and G. Rastelli, Decoherence and relaxation of topological states in extended quantum Ising models, SciPost Phys. **6**, 037 (2019).

[19] A. Kitaev, Unpaired Majorana fermions in quantum wires, Phys. Usp. **44**, 131 (2001).

[20] M. Leijnse and K. Flensberg, Introduction to topological superconductivity and Majorana fermions, Semicond. Sci. Technol. **27**, 124003 (2012).

[21] A. A. Zvyagin, Possibility of Direct Observation of Edge Majorana Modes in Quantum Chains, Phys. Rev. Lett. **110**, 217207 (2013).

[22] M. Greiter, V. Schnells, and R. Thomale, The 1D Ising model and the topological phase of the Kitaev chain, Ann. Phys. **351**, 1026 (2014).

[23] Y. Niu, S. B. Chung, C. H. Hsu, I. Mandal, S. Raghu, and S. Chakravarty, Majorana zero modes in a quantum Ising chain with longer-ranged interactions, Phys. Rev. B **85**, 035110 (2012).

[24] N. Read and D. Green, Paired states of fermions in two dimensions with breaking of parity and time-reversal symmetries and the fractional quantum Hall effect, Phys. Rev. B **61**, 10267 (2000).

[25] G. Zhang and Z. Song, Topological Characterization of Extended Quantum Ising Models, Phys. Rev. Lett. **115**, 177204 (2015).

[26] G. Zhang, C. Li, and Z. Song, Majorana charges, winding numbers and Chern numbers in quantum Ising models, Sci. Rep. **7**, 8176 (2017).

[27] M. W. Y. Tu and W. M. Zhang, Non-Markovian decoherence theory for a double-dot charge qubit, Phys. Rev. B **78**, 235311 (2008).

[28] J. S. Jin, M. W. Y. Tu, W. M. Zhang, and Y. J. Yan, Non-equilibrium quantum theory for nanodevices based on the Feynman-Vernon influence functional, New J. Phys. **12**, 083013 (2010).

[29] H. N. Xiong, W. M. Zhang, X. G. Wang, and M. H. Wu, Exact non-Markovian cavity dynamics strongly coupled to a reservoir, Phys. Rev. A **82**, 012105 (2010).

[30] M. H. Wu, C. U. Lei, W. M. Zhang, and H. N. Xiong, Non-Markovian dynamics of a microcavity coupled to a waveguide in photonic crystals, Opt. Express **18**, 18407 (2010).

[31] W. M. Zhang, P. Y. Lo, H. N. Xiong, M. W. Y. Tu, and F. Nori, General Non-Markovian Dynamics of Open Quantum Systems, Phys. Rev. Lett. **109**, 170402 (2012).

[32] C. U. Lei and W. M. Zhang, A quantum photonic dissipative transport theory, Ann. Phys. **327**, 1408 (2012).

[33] P. Y. Yang, C. Y. Lin, and W. M. Zhang, Master equation approach to transient quantum transport in nanostructures

incorporating initial correlations, Phys. Rev. B **92**, 165403 (2015).

[34] P. Y. Yang and W. M. Zhang, Buildup of Fano resonances in the time domain in a double quantum dot Aharonov-Bohm interferometer, Phys. Rev. B **97**, 054301 (2018).

[35] H. L. Lai, P. Y. Yang, Y. W. Huang, and W. M. Zhang, Exact master equation and non-Markovian decoherence dynamics of Majorana zero modes under gate-induced charge fluctuations, Phys. Rev. B **97**, 054508 (2018).

[36] A. Osterloh, L. Amico, G. Falci, and R. Fazio, Scaling of entanglement close to a quantum phase transition, Nature (London) **416**, 608 (2002).

[37] T. J. Osborne and M. A. Nielsen, Entanglement in a simple quantum phase transition, Phys. Rev. A **66**, 032110 (2002).

[38] G. Vidal, J. I. Latorre, E. Rico, and A. Kitaev, Entanglement in Quantum Critical Phenomena, Phys. Rev. Lett. **90**, 227902 (2003).

[39] P. Calabrese and J. Cardy, Entanglement entropy and quantum field theory, J. Stat. Mech. (2004) P06002.

[40] Y. Hatsugai, Chem Number and Edge States in the Integer Quantum Hall Effect, Phys. Rev. Lett. **71**, 3697 (1993).

[41] M. Ezawa, Y. Tanaka, and N. Nagaosa, Topological Phase Transition without Gap Closing, Sci. Rep. **3**, 1790 (2013).

[42] R. P. Feynman and F. L. Vernon, The theory of a general quantum system interacting with a linear dissipative system, Ann. Phys. **24**, 118 (1963).

[43] A. O. Caldeira and A. J. Leggett, Path integral approach to quantum Brownian motion, Physica A **121**, 587 (1983).

[44] L. Amico, R. Fazio, A. Osterloh, and V. Vedral, Entanglement in many-body systems, Rev. Mod. Phys. **80**, 517 (2008).

[45] E. Canovi, E. Ercolessi, P. Naldesi, L. Taddia, and D. Vodola, Dynamics of entanglement entropy and entanglement spectrum crossing a quantum phase transition, Phys. Rev. B **89**, 104303 (2014).